University of Alabama in Huntsville
LOUIS

Theses | UAH Electronic Theses and Dissertations

2024

The effects of reducing carbon content in the processing of superalloy Inconel 718

Glenn "Joey" Scott

Follow this and additional works at: https://louis.uah.edu/uah-theses

Recommended Citation
Scott, Glenn "Joey", "The effects of reducing carbon content in the processing of superalloy Inconel 718" (2024). *Theses*. 689.
https://louis.uah.edu/uah-theses/689

This Thesis is brought to you for free and open access by the UAH Electronic Theses and Dissertations at LOUIS. It has been accepted for inclusion in Theses by an authorized administrator of LOUIS.

THE EFFECTS OF REDUCING CARBON CONTENT IN THE PROCESSING OF SUPERALLOY INCONEL 718

Glenn "Joey" Scott

A THESIS

Submitted in partial fulfillment of the requirements
for the degree of Master of Science
in
Materials Science
to
The Graduate School
of
The University of Alabama in Huntsville
August 2024

Approved by:

Dr. Judith Schneider, Research Advisor & Committee Chair
Dr. Jeffrey Weimer, Committee Member
Dr. Nathan Spulak, Committee Member
Dr. Judith Schneider, Program Director
Dr. Jon Hakkila, College Dean
Dr. Jon Hakkila, Graduate Dean

Abstract

THE EFFECTS OF REDUCING CARBON CONTENT IN THE PROCESSING OF SUPERALLOY INCONEL 718

Glenn "Joey" Scott

A thesis submitted in partial fulfillment of the requirements for the degree of Master of Science

Materials Science

The University of Alabama in Huntsville
August 2024

The properties of Inconel 718 (IN718) are dependent on the elemental composition and microstructure. Applications using IN718 include rocket and jet engine parts. These parts are often complex and difficult to machine, making IN718 ideal for additive manufacturing processes such as laser-powder bed fusion (L-PBF). The various phases that form in IN718 rely on the niobium (Nb) content including the carbides. The precipitates also include Nb in the strengthening phases of gamma prime (γ') and gamma double prime (γ''). Overaging of γ'' transforms the metastable phase into the stable (δ) phase, which also controls grain size. This study evaluates the effects of reducing carbon content on phases and properties of IN718.

Acknowledgements

I would first like to thank my advisor Dr. Judith Schneider for her dedication to her craft and passion for creating future leaders of character. Her patience is unparalleled, and her guidance is what made me successful in all my grad school endeavors. I would also like to thank my parents and family, Guy, Rosemary, Robert, and Billy Scott for their unwavering support. I would be remised if I didn't thank Slothrust (Leah Wellbaum and Will Gorin), Titus Andronicus (Patrick Stickles), and Through Arteries (Cory Brunnemann). The countless nights of listening to your music while drinking coffee (way too late) kept me sane and focused. To Rex Hausmann: you have been telling me to pursue grad school for about 10 years now and you planted that seed. Remember, the garden will grow where it is planted. Frank Allen, I believe in you and know you can deadlift and squat 1,000 lbs. I also need to thank Isaac Barnett, Elaina Walker, Michael Santangelo, Brody Montgomery, Japheth Hayman, Sebastian Rivera, Swinson Terry, and Peyton Hall for being great friends and groupmates. Thank you all for pushing me to be successful.

I could not have done this without the support from NASA Marshall Flight Center. Personally, I would like to thank Gabe Demeneghi, Kristina Rodgers, Ellen Rabenberg, Sid Gorti, Matt Medders, and Colton Katsarelis for your friendship and support. I would also like to thank Mr. David B Witkin at Aerospace Corporation for providing the samples.

Funding for my graduate degree was provided by the US Army. I want to thank my former leadership, specifically COL Matt Tedesco, COL Doug Waddingham, COL Jim Reese, Mr. Kevin Parker, LTC Mike Krayer, LTC Brandon Prisock, and LTC Noah Tartal for always having the faith in me to complete this mission.

Table of Contents

Abstract ii

Acknowledgements iv

Table of Contents v

List of Figures vii

List of Tables ix

List of Symbols x

Chapter 1. Introduction 1

1.1 Introduction 1

1.2 Additive Manufacturing 1

1.3 Laser Powder Bed Fusion 4

Chapter 2. Background 6

2.1 Inconel 718 6

2.2 Alloying Elements and Phases Present 6

2.3 Heat Treatments 9

2.4 Carbon in IN718 11

Chapter 3. Experimental Procedure 13

3.1 Feedstock 13

3.2 Sample Fabrication 14

3.3 Metallurgical Preparation 15

3.4 Hot Isostatic Pressing and Heat Treatments 16

3.5 Optical Microscopy 17

3.6 Tensile Testing 18

3.7 X-ray Diffraction 19

3.8 Scanning Electron Microscopy 19

Chapter 4. Results 20

4.1 Hot Isostatic Pressing and Heat Treatment 20

4.2 Tensile Testing Results 28

4.3 Phase Analysis Results 28

Chapter 5. Discussion 35

Chapter 6. Summary 40

Chapter 7. Future Work 42

References 44

List of Figures

Figure 1.1 Overview scheme on AM processes.....3

Figure 1.2 Feature resolution vs. deposition rate of various AM processes.....3

Figure 1.3 Principle schematic of L-PBF.....5

Figure 1.4 Major processing parameters involved in L-PBF 5

Figure 2.1 Ternary phase diagram for Fe, Ni, Cr at 750C 8

Figure 2.2 TTT diagram for wrought IN718.....10

Figure 3.1 Build plate with build directions schematic 14

Figure 3.2 Vertical and horizontal specimens used in current study 15

Figure 3.3 Cut plane schematic.....15

Figure 3.4 Specimens mounted in phenolic mounting resin.....16

Figure 3.5 Heat treatment schedule applied to TTT diagram 17

Figure 3.6 Tensile sample geometry with dimensions 18

Figure 4.1 SEM/BSE images (100x) lean C specimens XY build plane (a) horizontal and (b) vertical build 21

Figure 4.2 SEM/BSE image (100x) of microstructure of baseline HT vertical build IN718 specimen in XY build plane 22

Figure 4.3 SEM/BSE images (1500x) of delta phase and carbides in XY plane for IN718 specimens (a) baseline vertical (b) lean C horizontal (c) Lean C vertical 24

Figure 4.4 SEM/BSE images (5000x) of lean C specimens XY plane with coarse acicular δ phase formation at grain boundaries for (a) horizonal and (b) vertical. 25

Figure 4.5 SEM/BSE image (5000x) of baseline HT specimen XY build plane with acicular δ phase formation at grain boundaries 26

Figure 4.6 Optical microscopy images for void analysis of (a) baseline HT vertical and (b) lean C HT vertical 27

Figure 4.7 Mechanical properties for IN718 specimens 28

Figure 4.8 XRD analysis of IN718 (a) as built and (b) HT.....30

Figure 4.9 XRD analysis for Ni peak for IN718 (a) as built and (b) HT 31

Figure 4.10 XRD analysis for NbC peak for IN718 (a) as built and (b) HT 32

Figure 4.11 XRD analysis for Laves peak for IN718 (a) as built and (b) HT 33

Figure 4.12 XRD analysis for δ phase peak for IN718 (a) as built and (b) HT 34

List of Tables

Table 2.1 Standard elemental composition (wt%) of IN718 7

Table 2.2 Elements and their effects in IN718 7

Table 2.3 Phases present and crystal structures in IN718 9

Table 2.4 Typical heat treatments for L-PBF for IN718 11

Table 3.1 Chemical composition (wt%) of IN718 powder and bulk used in current study 13

Table 3.2 Heat treatment schedule 16

Table 4.1 Average grain size after HT for IN718 Specimens 20

Table 4.2 Summary of void analysis after HT for IN718 specimens 26

Table 4.3 Mechanical properties for Inconel specimens 28

Table 4.4 ICDD PDF numbers for corresponding phase 29

List of Symbols

Symbol	Description
AM	Additive Manufacturing
BCT	Body Centered Tetragonal
BJ	Binder Jetting
DED	Direct Energy Deposition
D	Grain Size
EB-PBF	Electron Beam Powder Bed Fusion
FC	Furnace Cooling
FCC	Face Centered Cubic
H-P	Hall Petch
HPC	Hexagonal Close Packed
HIP	Hot Isostatic Pressing
ICDD	International Center for Diffraction Data
ICP	Inductively Coupled Plasma
IN718	Inconel 718
k	H-P Slope
LCF	Low Cycle Fatigue
LOM	Laminated Object Manufacturing
L-PBF	Laser Powder Bed Fusion
MAM	Metal Additive Manufacturing
MC	Metal Carbide
MPa	Megapascal
SDD	Silicon Drift Detector

SEM	Scanning Electron Microscopy
SL	Stereolithography
SLA	Stereolithography Apparatus
SLM	Selective Laser Melting
SR	Stress Relief
TTT	Time, Temperature, and Transformation diagram
UTS	Ultimate Tensile Strength
XRD	X-ray diffraction
YAG	yttrium aluminum garnet
YS	Yield Strength
δ	Delta phase
γ	Gamma phase
γ'	Gamma prime phase
γ''	Gamma double prime phase
σ_0	Frictional Stress
σ_y	Yield Strength

Chapter 1. Introduction

1.1 Introduction

Understanding phase formation and microstructures associated with elemental composition is important for designing a material to meet desired mechanical properties. In Inconel 718 (IN718), phases form in either solidification or precipitation. The precipitates are gamma prime (γ'), gamma double prime (γ''), delta (δ), Laves, and carbides, while solidification phases, are the gamma (γ) matrix, δ, Laves, and carbides. Both solidification and precipitation phases have been observed in cast, wrought, and additively manufactured (AM) materials [1][2][3]. Laves and δ phases can be detrimental in large quantities to the overall strength of the material. Heat treatments above phase solvus temperatures are used to help minimize those phases [2][3].

The objective of this research is to determine the effects on the phase formation and mechanical properties of reducing carbon content in IN718. Test specimens were printed with either a baseline or lean carbon content and heat treated using HIP prior to solutionizing and aging. The baseline carbon content is .04 weight percent, and the lean carbon content is .01 weight percent in the powder used for fabrication. The resulting microstructures, phase compositions, and mechanical properties are presented in this thesis.

1.2 Additive Manufacturing

AM is the process of joining materials to make parts from 3D model data, usually layer upon layer, as opposed to subtractive or formative manufacturing methodologies [4][5][6]. AM can be a cost-effective and time saving alternative to other subtractive

process to produce and manufacture low volume, complex parts. Some of the complexities cannot be produced using traditional subtractive processes. AM first emerged in the late 1980's with stereolithography (SL) from 3D Systems, with a process that solidified polymers [5]. The first commercially available 3D printer was the SLA-1 (Stereolithography Apparatus), which became commercially available in 1987, with the printer being patented in 1984 to Chuck Hull [7][8]. Hull was one of the founders of 3D systems [7]. In 1993, the Massachusetts Institute of Technology first patented, three-dimensional printing techniques, that would be defined as binder jetting (BJ). [6][9]. Since that point, AM has made significant strides with the use of metals [6].

Classifications of AM can be reduced to many different categories which are shown in Figure 1.1. The processes can be broken down by material. The following processes are primarily used for metals: Selective Laser Melting (SLM), Direct Energy Deposition (DED), Laminated Object Manufacturing (LOM), and BJ [10]. The method used to produce the specimens in this study is SLM which is now standardized as Laser Powder Bed Fusion (L-PBF) [4].

Figure 1.2 shows the metal additive manufacturing (MAM) processes categorized based on their heat source and feedstock. There is an inverse relationship between precision (or resolution) and deposition rate [11]. With PBF systems, the heat source is either laser (L-PBF) or electron beam (EB-PBF). Due to difficulties in the machining of IN718, it is an ideal material for any of the MAM processes, depending on design requirements.

Process	Acronyms	Feedstock	Material	Bonding and join
Extrusion (or fused filament fabrication or fused deposition modeling)	FFF, FDM	Filament, rod, pellets	Polymer	Fused with heat
Photopolymerization (or stereolithography)	SLA	Liquid	Photopolymer, metal, ceramics, composite	Cured with laser, projector, UV light
Material Jetting (or Binder Jetting)	MJ (BJ)	Powder, liquid	Ceramic, wax, polymer, metal, sand	Cured with UV light, heat
Laminated Object Manufacturing (or Sheet Lamination)	LOM	Sheet	Paper, metal, polymer	Joined with agent, heat and pressure
Selective Laser Melting	SLM	Powder	Metal	Fused with laser and electron beam
Directed Energy Deposition	DED, EBM	Wire, powder	Metal	Fused with laser and electron beam

Figure 1.1 Overview scheme on AM processes [10].

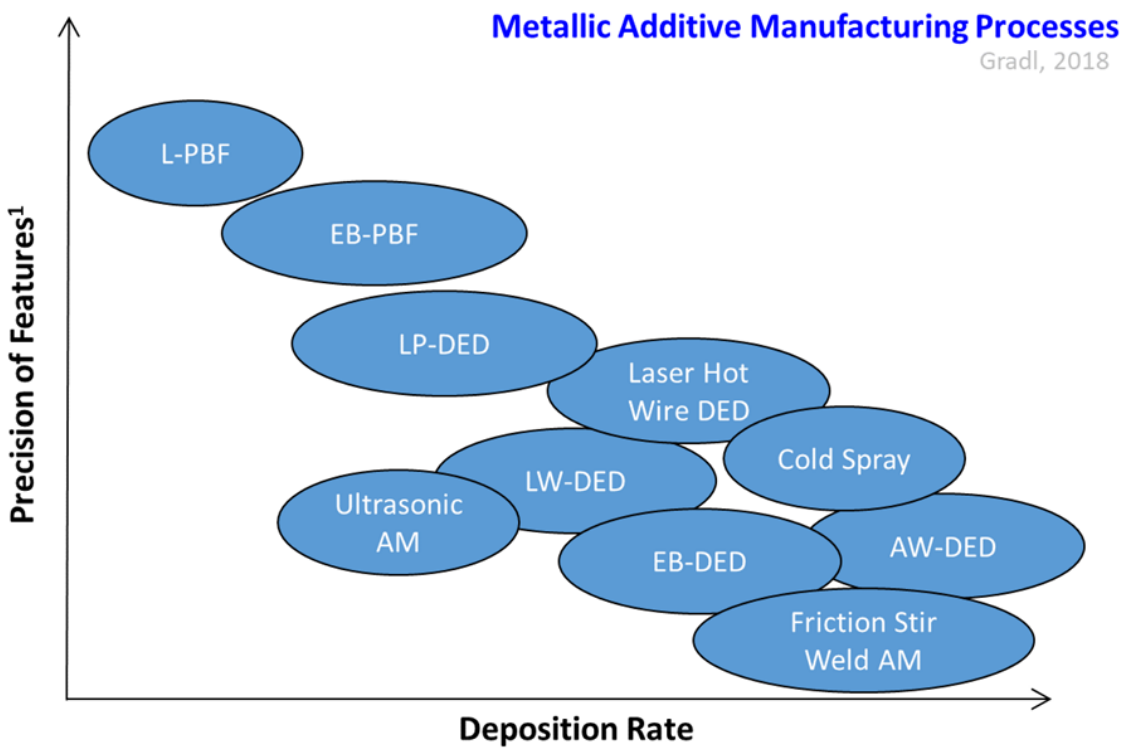

Figure 1.2 Feature resolution vs. deposition rate of various AM processes [11].

1.3 Laser Powder Bed Fusion

One form of MAM is L-PBF. Since its application to metal processing, it has gone through a variety of names including using SLM prior to standardization as L-PBF [4]. AM processing enables the ability to produce complex geometries, reduce part counts, improve economics of small production runs, and dramatically reduce lead times in production environments [12][13]. L-PBF is under widespread development due to its capacity for improved quality and freedom in designing and manufacturing complex geometries [12].

Figure 1.3 shows the principal schematic for L-PBF. L-PBF uses a laser (heat source) that is scanned across a layer to selectively melt and consolidate metal powder. Once that layer is scanned, an additional layer of powder is spread across the previous layer to form the successive layers. This process is repeated to create three-dimensional layered components with internal features that are difficult to attain through traditional manufacturing [12][14].

Figure 1.4 illustrates the five main parameters that control the process including: laser power, layer thickness, laser scan speed, hatch distance, and scan strategy [15]. Laser power is the amount of power (heat) the laser imparts on the surface of the build plate or specimen being built. Layer thickness is the thickness of each individual layer of powder melted and solidified by the laser. Laser scan speed is the scanning velocity, or how fast the laser is moving. Hatch distance is the distance between each laser scan pass over the specimen. Scan strategy is the pattern or path the laser takes while it scans. Laser processing conditions can be optimized to enhance desired mechanical properties [16].

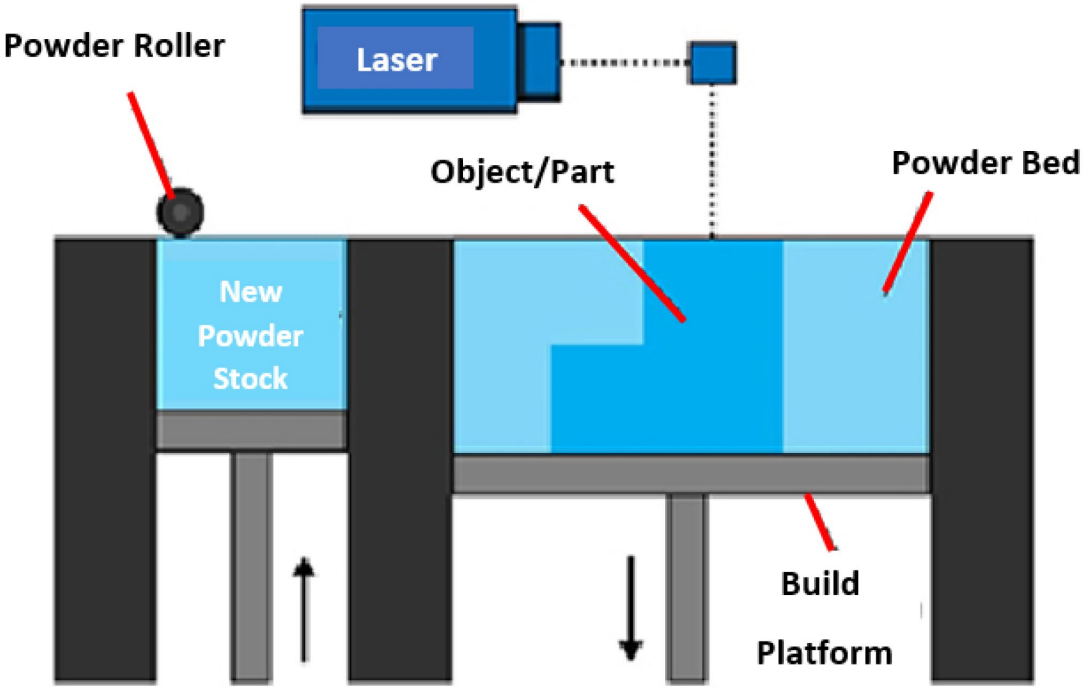

Figure 1.3 Principle schematic of L-PBF [17].

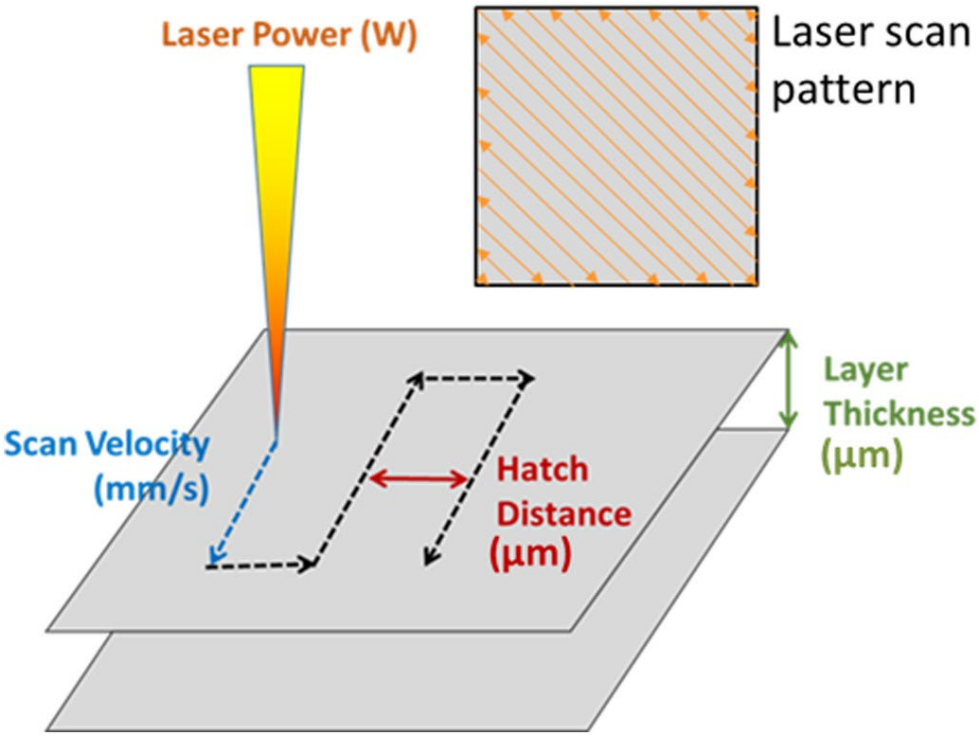

Figure 1.4 Major processing parameters involved in L-PBF [15].

Chapter 2. Background

2.1 Inconel 718

The Inconel family of materials was first developed in the early 1930's by the International Nickel Company and IN718 was announced in 1959, with its first public issuance was in March 1962 [18]. IN718 was developed to be a high strength, creep resistant, and corrosion resistant material that could operate successfully in temperatures up to 650° C [1][19]. Above 650° C, γ'' becomes unstable and transforms into δ phase [3][18]. IN718 was first developed to be used in jet engines. Now it is used in many applications where strength retention is needed at higher temperatures and/or in a corrosive environment. IN718 is highly weldable due to sluggish precipitation kinetics [20]. IN718 can also be used in wrought or casting processing, as well as additive manufacturing [21].

2.2 Alloying Elements and Phases Present

IN718 is an austenitic Ni based superalloy that is precipitation strengthened. It is composed of the elements listed in Table 2.1. While most are intentional alloying elements, some others are left as impurities such as oxygen, nitrogen, phosphorus, and sulfur. The major alloying elements are given within the stated range.

Table 2.2 shows why each element is added to the composition of IN718. For example, the Cr present in IN718 provides oxidation resistance by forming a passive layer of chromium oxide (Cr_2O_3) [22].

Table 2.1 Standard elemental composition (wt%) of IN718 [23].

Element	min	max
Nickel	50	55
Chromium	17	21
Iron		bal
Niobium + Tantalum	4.75	5.5
Molybdenum	2.8	3.3
Titanium	0.65	1.15
Aluminum	0.2	0.8
Cobalt		1
Manganese		0.35
Silicon		0.35
Carbon		0.08
Oxygen		0.01
Phosphorus		0.015
Sulfur		0.015
Copper		0.3
Boron		0.006

Table 2.2 Elements and their effects in IN718 [1][3][20][22][24][25][26].

Element	Effects
Ni	Primary element in austenitic γ matrix
Cr	Solid-solution strengthener, M_7C_3 and $M_{23}C_6$ carbides former, improve oxidation and hot corrosion resistance
Fe	Solid-solution strengthener
Nb	Strengthening phase γ″ Ni_3Nb, MC and M_6C carbides former
Mo	Solid-solution strengthener, MC, $M_{23}C_6$ and M_6C carbides former
Ti	Strengthening phase γ′ Ni3(Al,Ti) former
Al	Strengthening phase γ′ Ni3(Al,Ti) former, improve oxidation and hot corrosion resistance
Co	Solid-solution strengthener, raises solvus temperature of γ' Ni_3(Al,Ti)
Mn	Stabilize austenitic γ matrix, increase weldability
Si	Promote effect of solidification segregation
C	M(C,N) carbonitrides former, carbide former, grain-boundary strengthener
O	Contaminant and present in the powder during LPB-F

Table 2.3 lists the phases present in IN718 include an austenitic γ matrix, γ', γ'', δ phase, Laves, and carbides [27]. The γ matrix is the primary phase present, and it retains

its FCC structure over the entire temperature range through alloying with the Fe and Cr elements. Figure 2.1 is the ternary diagram for Fe, Ni, and Cr at 750°C, showing the compositional range for the stability of the γ matrix, which is Ni 50-55, Cr, 17-21, and Fe 17-21 wt% [23].

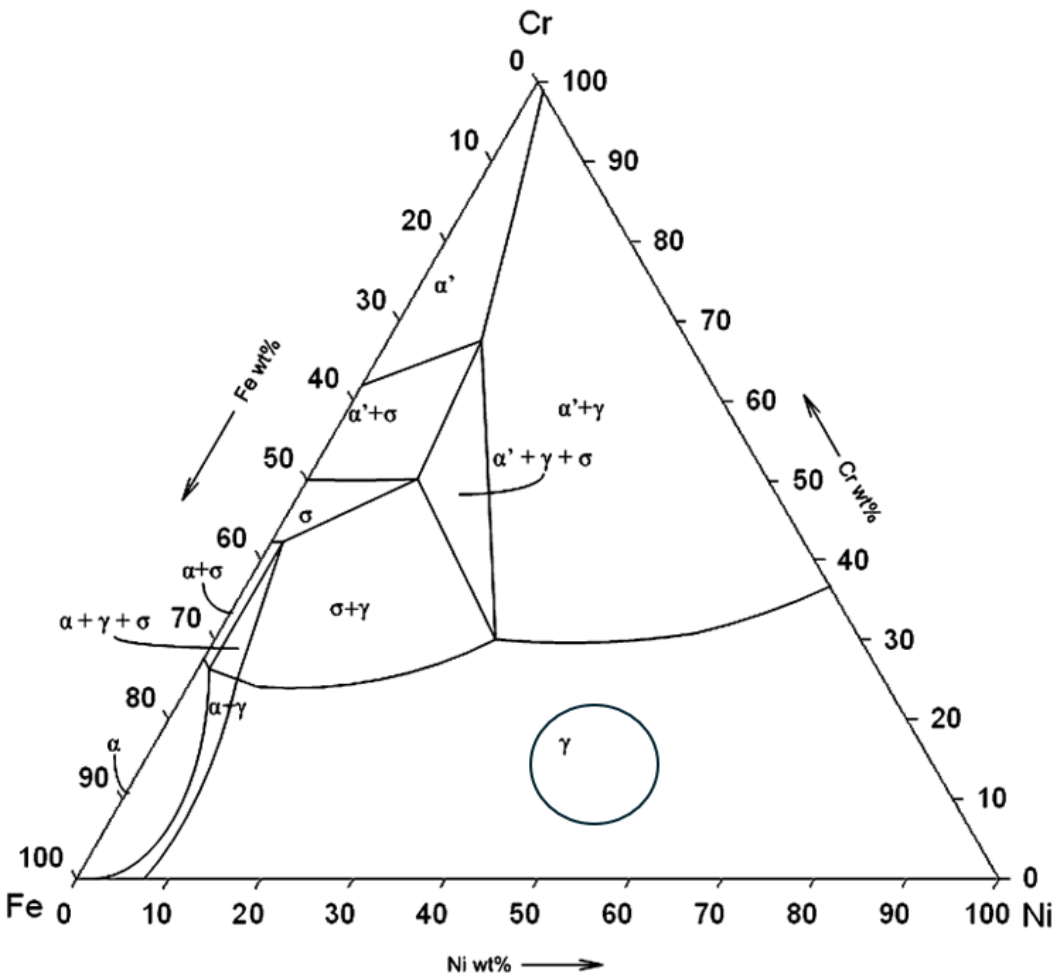

Figure 2.1 Ternary phase diagram for Fe, Ni, Cr at 750° C showing compositional ranges [28].

Table 2.3 lists the crystallographic structure, composition, and primary function of phases within IN718. γ' and γ" are the primary strengthening precipitates with γ" forming alongside γ' [29]. γ" is a metastable phase with a BCT structure that remains coherent with the γ matrix. At temperatures above 650° C, the γ" transforms to the stable δ phase that has

an orthorhombic crystal structure and is incoherent with the γ matrix. It can form in either globular and/or acicular morphologies, usually along the grain boundaries [20]. The δ phase is useful in pinning grain boundaries to inhibit grain growth [20].

The other phases are Laves phase and carbides. Laves phase has a topographical hexagonal close packed (HCP) crystal structure and in large amounts can be detrimental to the matrix. Laves phase tends to be initiation sites for cracks thereby impacting low cycle fatigue (LCF) life [20]. Carbides can be either precipitates or occur in solidification. When carbides are precipitates, carbides precipitate throughout the matrix and/or along the grain boundaries where they can also pin grain boundaries [20]. Carbides are useful for grain size control but can be detrimental in too high of volume fractions.

Table 2.3 Phases present and crystal structure in IN718 [1][3][18][29][30].

Phase	Structure	Composition	Formation
Gamma (γ)	Face Centered Cubic (FCC)	Ni,Cr,Fe	Solid Solution Matrix
Gamma prime (γ')	Ordered Face Centered Cubic (FCC)	$Ni_3(Al,Ti,Nb)$	Metastable Intermetallic
Gamma double prime (γ'')	Body Centered Tetragonal (BCT)	$Ni_3(Nb,Ti)$	Metastable Intermetallic
Delta (δ)	Orthorhombic	$(Ni_3(Nb,Ti)$	Intermetallic
Laves	Hexagonal Topographical Close Packed (TCP	$(Ni,Cr,Fe)_2(Nb,Ti)$	Intermetallic
Carbides	Cubic	NbC	

2.3 Heat Treatments

Due to the complex nature and thermal cycling involved with AM processing, postproduction heat treatments are necessary to get the optimal mechanical properties. For L-PBF processing, a stress relief (SR) cycle can be used to minimize distortion of the part

when removing from the build plate, especially for thin walls [31]. Due to the rapid cooling, a homogenization heat treatment is used to homogenize the material by diffusing the elemental segregation. For precipitation strengthened alloys, additional heat treatments are used to solutionize followed by a quench and an aging to strengthen the material [31].

Figure 2.2 shows the isothermal time, temperature, and transformation (TTT) diagram for wrought IN718. The TTT diagram provides an understanding of the time and temperature ranges where the various phases form and precipitate.

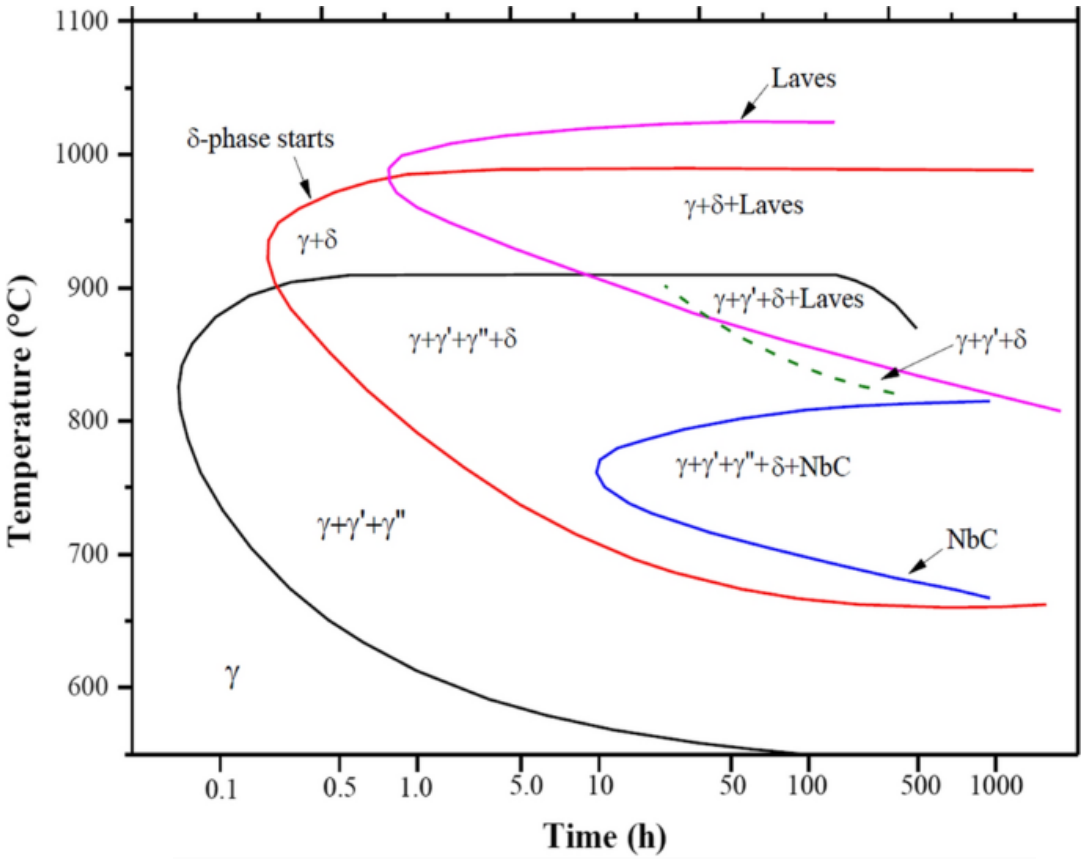

Figure 2.2 Time, Temperature, and Transformation (TTT) diagram for wrought IN718 [32].

The basic heat treatment for IN718 was developed for wrought and cast materials. But for L-PBF IN718, there has been the addition of stress relief (SR) and hot isostatic pressing (HIP), per AMS F3055 [23]. As the AM process may add residual to the material due to the temperature gradient during the build, the additional SR was added to minimize

distortion in the as built AM components, especially for thin-walled components. HIP processing, common to casting, is used to reduce the void content arising during solidification, consequently increasing the density. Table 2.3 shows the standard heat treatment typically used for L-PBF IN718 [23][33].

Understanding the appropriate parameters of the TTT diagram helps form a basis for designing the appropriate heat treatment. For IN718, the two-step aging promotes the formation of γ' and γ" at a range of 718°C to 760°C for 8 hours [33]. To continue the formation of these phases, the temperature is reduced to a range of 621°C to 641°C for an additional 8 hours, to continue the formation of the strengthening phases and delay the formation of δ phase [31]. Per the standard, the total aging time, including cooling, is not to exceed 18 hours [33].

Table 2.4 Typical heat treatment of LPB-F IN718 [23][33].

Heat Treatment	Temperature (°C) / Time (hr)	Pressure (MPa)
Stress Relief [23]	1065 °C ± 15°C 1.5 hr -5 min/+15 min	NA
HIP [23]	1120 °C – 1185 °C ± 15°C 4 hr ± 1 hr	100 MPa
Solution [33]	941°C – 1010 °C ± 14 °C 1-2 hr, quench	NA
Age [33]	718 °C -760 °C ± 15°C 8 hr	NA
Second Aging [33]	621 °C – 641 °C / approx 8 hr	NA

2.4 Carbon in IN718

According to UNS N07718, the maximum carbon content allowed in IN718 is .08 wt% [23][34]. Although the maximum C allowed is .08 wt%, commercially available IN718 powder typically has .04 wt% C [35]. The initial .08 wt% C content was developed

for wrought and castings [1][3][36]. The primary driving force for reducing the carbon content to .04 wt% is improving LCF life [37]. Cracks generally occur at oxide, nitride, and carbide stringer sites. Reducing the C decreases the amount of carbide stringer sites present, and consequently improving LCF life [37].

Although too much C can be detrimental, the primary use of C in IN718 is to produce carbides, primarily with niobium and secondarily with titanium or aluminum [27][34]. Carbides can form during solidification and/or also after solutionizing heat treatments [21][38]. The stable form of carbide is a metal-carbide, MC. In Inconel, the primary MC is NbC and the formation of NbC follows normal thermodynamic relationships [38].

The MC carbides that form during solidification tend to form along the austenitic grain boundaries [20][38]. Carbides can precipitate along twin boundaries [20]. The distribution of carbides is nonuniform [27]. In IN718, NbC is the primary while $M_{23}C_6$ can also form [20]. Whereas other carbides such as M_6C occur in IN625, they do not occur regularly in IN718 [20]. Carbides being beneficial or detrimental to mechanical properties depend on the size, distribution, oxidation, and mechanical test conditions [39].

Chapter 3. Experimental Procedure

3.1 Feedstock

The Inconel718 powder that was used in this study had nominal diameter of 10 µm to 50 µm [24]. The mean particle size in the powder used was 34.1 µm, with a D10 size of 23.1 µm and a D90 with a size of 46.1 µm [40]. That is to say that 90% of the powder had a diameter larger than 23.1 µm and 90% of the powder had a diameter smaller than 46.1 µm. The manufacturer's independent powder analysis showed that their as-received powder met AMS 5662 nominal composition limits for IN718 [34].

Table 3.1 summarizes the chemical compositions for all powder and specimens used in this study that were provided by the vendor. The vendor determined the values by inductively coupled plasma (ICP) and combustion characterization techniques [41][42].

Table 3.1 Chemical composition (wt%) of IN718 powder and bulk used in current study [35].

Sample	Ni	Cr	Fe	Nb	Mo	Ti	Al	Co	Mn	Si	C	O
Lean C Powder	53.5	18.0	18.9	5.0	3.0	0.95	0.56	0.00	0.02	0.04	**0.01**	0.01
Lean C Bulk	53.6	17.9	18.6	5.3	3.0	0.98	0.55	0.01	0.03	0.04	**0.01**	0.03
Baseline Powder	53.3	18.9	17.9	5.1	3.0	0.94	0.47	0.10	0.04	0.04	**0.04**	0.01
Baseline Bulk	52.6	18.9	18.4	5.2	3.1	0.97	0.51	0.10	0.04	0.05	**0.04**	0.02
Wrought	53.2	18.1	18.9	5.1	2.0	0.9	0.55	0.22	0.05	0.07	**0.04**	0.01

3.2 Sample Fabrication

All samples in this study were manufactured by the Aerospace Corporation, using a Concept Laser M2 SLM AM system, with no base plate heating. The SLM AM system is classification of a laser-powder bed fusion (L-PBF) process [4]. The Concept Laser M2 used a single 400-W YAG (yttrium aluminum garnet) continuous fiber laser with a wavelength of 1070 nm and an f-theta lens system with fixed optics and nominal spot size of 50 µm. The print parameters used a 180-watt laser setting and a scan rate of 600 mm/s for the bulk. For the contour layers, a reduced laser power of 160 W and a scan rate of 350 mm/s was used. Layer thickness was 30 µm. An argon purge gas was used with an island scanning strategy with 5 by 5 mm island size. Cylindrical samples were printed in both the vertical and horizontal positions with nominal dimensions of a 12.7 mm diameter by 90 mm length [40]. Figure 3.1 shows the build plate and build direction and Figure 3.2 shows the cylindrical specimens.

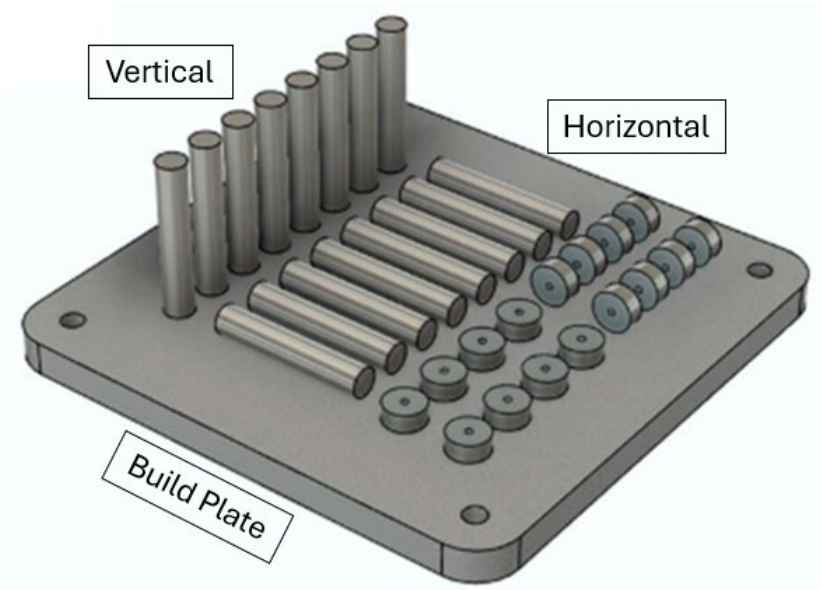

Figure 3.1 Build plate with build directions schematic [43].

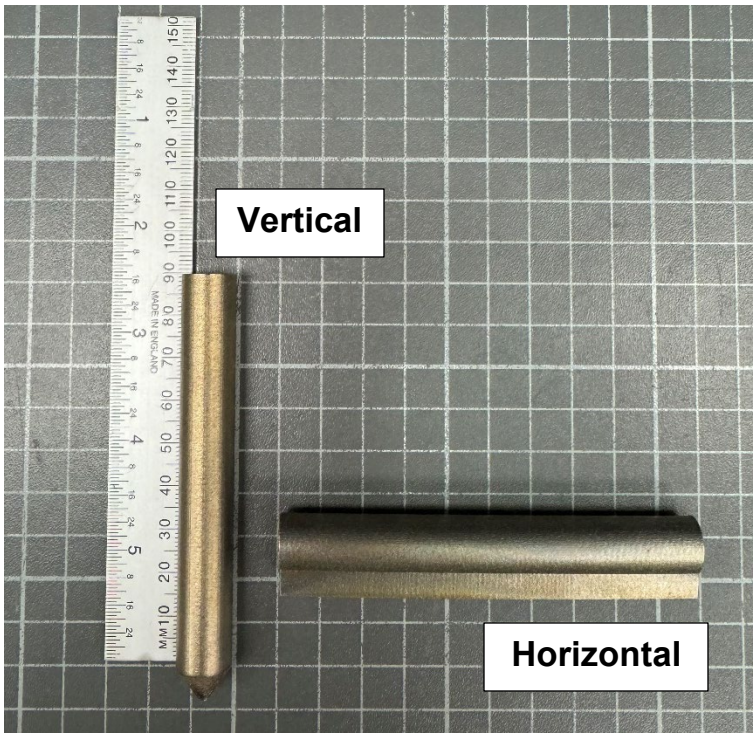

Figure 3.2 Vertical and horizontal specimens used in this study.

3.3 Metallurgical Preparation

To characterize the microstructure and their differences between the as built and heat treated conditions, the samples were cut and mounted at the University of Alabama in Huntsville, in phenolic to view the XY plane and XZ build directions, shown in Figure 3.3. Figure 3.4 shows an example of how they appeared in the black phenolic mounting resin.

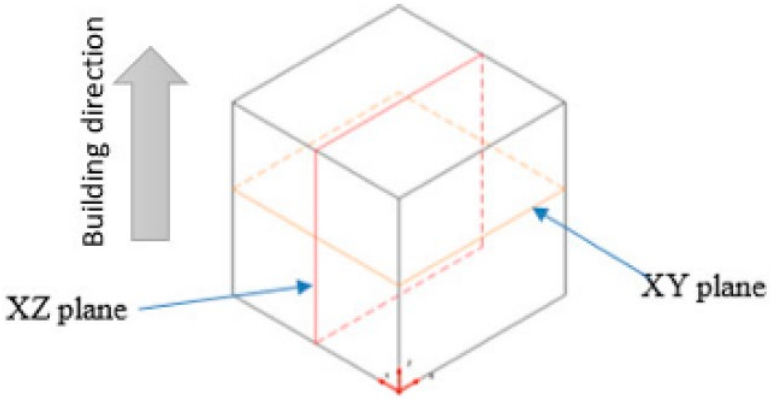

Figure 3.3 Cut plan Schematic for horizontal and vertical specimens [44].

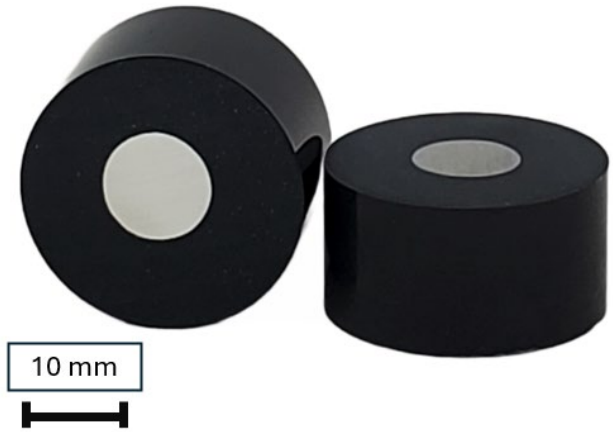

Figure 3.4 Specimens mounted in black phenolic mounting resin [45].

The samples were cut in the relative middle of their build to ensure that the maximal uniformity within the samples and alleviate anomalies at the baseplate. For characterization, the XY and XZ specimens were mounted into Allied High Tech black phenolic mounting resin, utilizing standard metallurgical techniques for IN718 [46]. The machine used for mounting is a Buehler SimpliMet 4000 mounting system for metallurgical preparation. After mounting, the samples were ground using a Struers Tegramin-20. The SiC grinding series started with 240 grit through to 1200 grit. The samples were then polished using a 1 μm diamond suspension polishing medium and a Vel-cloth pad.

3.4 Heat Treatments

Table 3.2 Heat treatment schedule [23][33].

Designation	Build Orientation	HIP (°C/hr)	Solution (°C/hr)	Age (°C/hr)	Second Aging (°C/hr)
Baseline	Vertical	1163/3 at 103 MPa	954/1 (FC*)	718/8	621/8 (FC*)
Lean	Vertical/Horizonal				

**FC = furnace cooled*

The specimens in this study were heat treated according to Table 3.2. The HIP cycle was run at1163 ± 12°C and 103 ± 2 MPa in an argon environment for 3 h, followed by a slow furnace cooling (FC). After the HIP processing, the test specimens underwent a two-step aging process per ASM 5663 [33]. Test specimens were solution treated for 1 h at 954 ± 14°C with air cool, followed by two-step aging at 718 ± 8°C for 8 h, followed by a furnace cool to 621 ± 8°C for 8 h, for a total aging time of 18 h. Figure 3.5 shows how the heat treatment is applied to the TTT diagram.

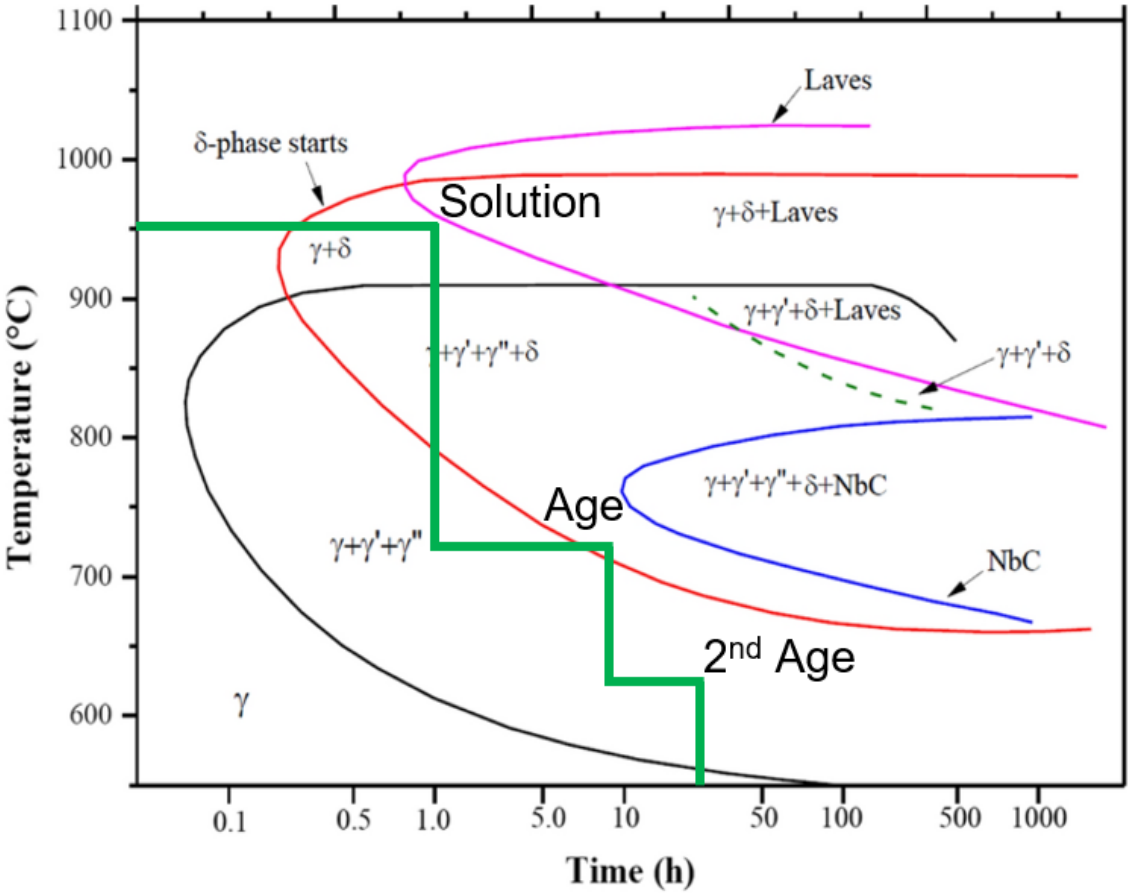

Figure 3.5 Heat treatment schedule applied to TTT diagram [32].

3.5 Optical Microscopy

Images of the polished samples were taken to conduct void analysis. The images were taken using a Zeiss AX10 inverted microscope at 5x, 10x, and 20x objective in the

XY build plane and the XZ build direction. Using the as polished samples in optical microscopy, sufficient imaged were recorded for an average of 100 voids using a 5x objective. Analysis was conducted using ImageJ for each representative sample after the specified heat treatment [47]. The process used in ImageJ was ensuring the image was 8-bit, threshold the image to void size, make the image binary, set measurements for area, feret diameter, and area fraction, lastly, analyze particles.

3.6 Tensile Testing

After the heat treatment schedule discussed in Section 3.4, the tensile specimens were machined into tensile samples per Figure 3.5 where dimensions are in mm. The samples printed in the vertical orientation were machined to align the tensile axis the build direction (Z) and those in the horizontal orientation were machined to align the tensile axis along the build plane (XY).

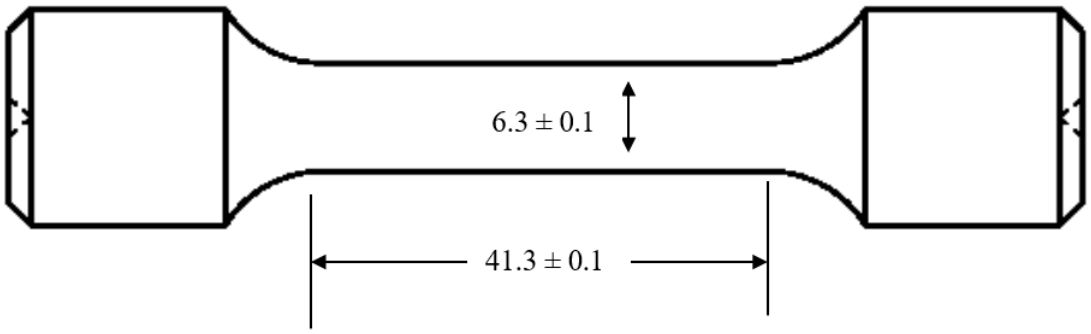

Figure 3.6 Tensile sample geometry with dimensions in mm.

The uniaxial tensile tests were conducted using an Instron 5985 with a 250 kN load cell in accordance with ASTM Standard E8/E8M [48]. The tensile tests were completed at room temperature on 19 dogbone specimens with a constant crosshead speed of 1.27

mm/min. All specimen gauge section diameters were between 6.29 mm and 6.39 mm.

3.7 X-Ray Diffraction

X-ray diffraction (XRD) was performed with a Malvern Panalytical Empyrean with a 255-channel detector on all specimens used in this study to determine the phase composition of each sample. XRD patterns were collected with an Empyrean diffraction system with Co-Kα radiation source ($\lambda = 0.179$ nm) operated at 40 kV and 40 mA over a continuous 2-θ range of 35 to 55°. The 2-θ range was scanned with a step size of 0.013 with a dwell time of 1200 seconds. No monochromator was installed on the XRD and the instrumental peak broadening was not measured. Thus, the measured peak widths were used to observe relative changes in peak width. One specimen from baseline HT vertical, lean C HT vertical, lean C HT horizontal, baseline as built vertical, and a lean C built horizontal was used.

3.8 Scanning Electron Microscopy

Scanning Electron Microscopy (SEM) was conducted using a Hitachi S-3700N. The Silicon Drift Detector (SDD) is a X-MaxN 80. Imaging was conducted using Backscattered Electron mode. Images of the specimens were taken at a resolution of 70x, 100x, 200x, 500x, 750x, and 1500x. The SEM images at a 100x magnification were used for the grain size analysis averaging 100 grains per sample. Using ImageJ, the feret diameter and aspect ratios were determined.

Chapter 4. Results

4.1 Hot Isostatic Pressing and Heat Treatment

Figure 4.1 compares the microstructure of the lean carbon HT samples from the horizontal and vertical build directions in the XY plane. Specimens were removed and mounted in accordance with the cut schematic in Figure 3.3. Figure 4.2 shows the microstructure of the baseline HT sample in the XY plane. Figure 4.3 compares details of the grain boundaries for lean HT and baseline HT samples. Figure 4.4 shows coarse delta formation at grain boundaries of lean C HT samples. Figure 4.5 shows less coarse acicular delta at grain boundaries in the baseline HT sample.

Table 4.2. summarizes the average grain size of HT specimens. An average of 100 grains per sample was used. One image in both XY and XZ planes were used with a resolution of 100x. Similar grain size in the two orientations are interpreted as evidence of equiaxed grains in the specimens.

Table 4.1 Average grain size after HT for IN718 specimens.

Sample	Number of Specimens	Grain Size XY	Grain Size XZ
Baseline Vertical	2	32 ± 24	33 ± 32
Lean C Vertical	2	54 ± 37	44 ± 28
Lean C Horizontal	2	25 ± 14	36 ± 21

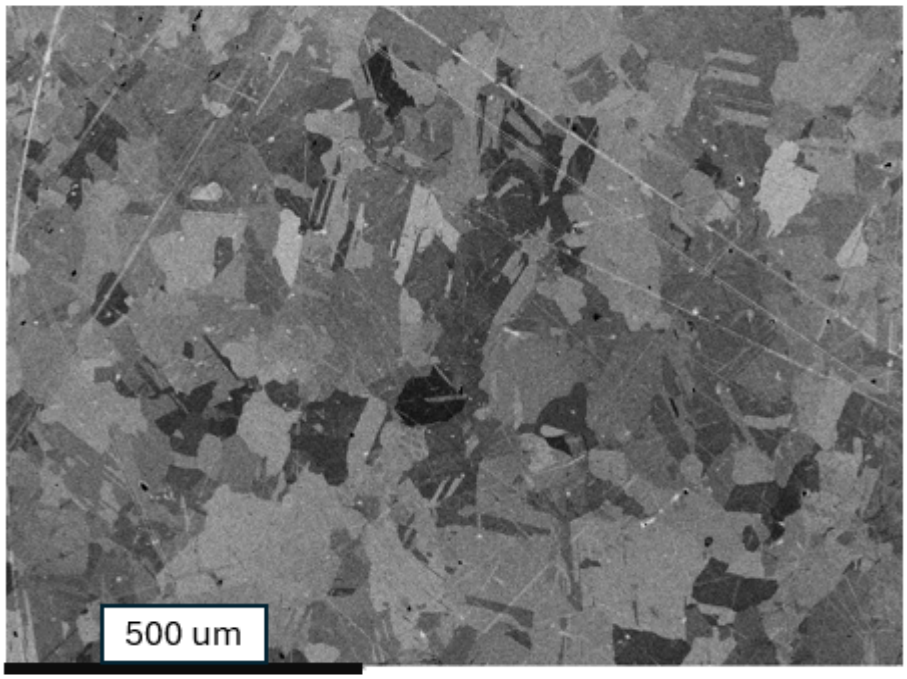

(a)

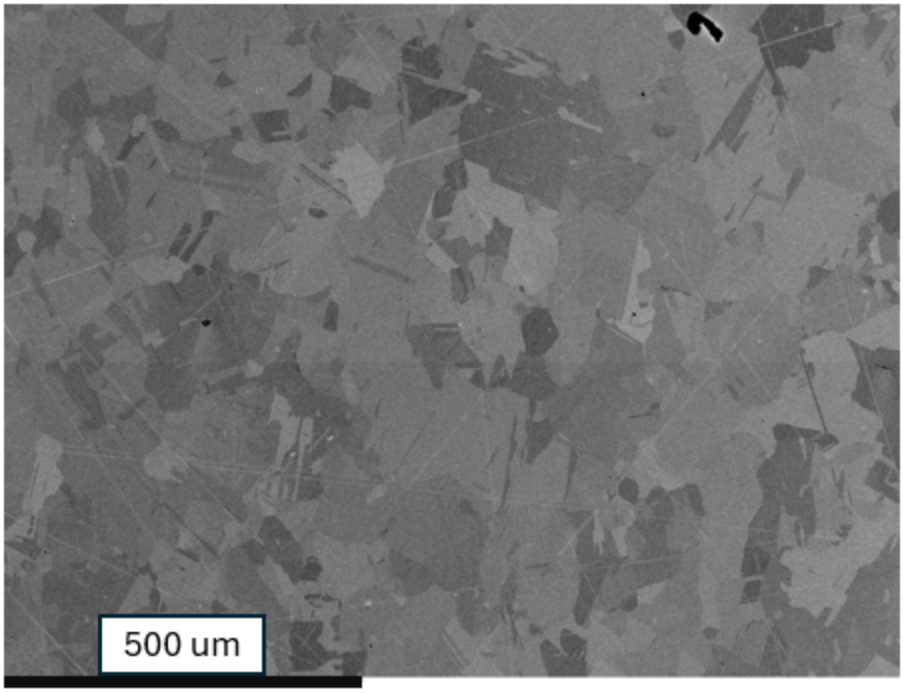

(b)

Figure 4.1 SEM/BSE images (100x) lean C HT specimens in XY plane (a) horizontal and (b) vertical build.

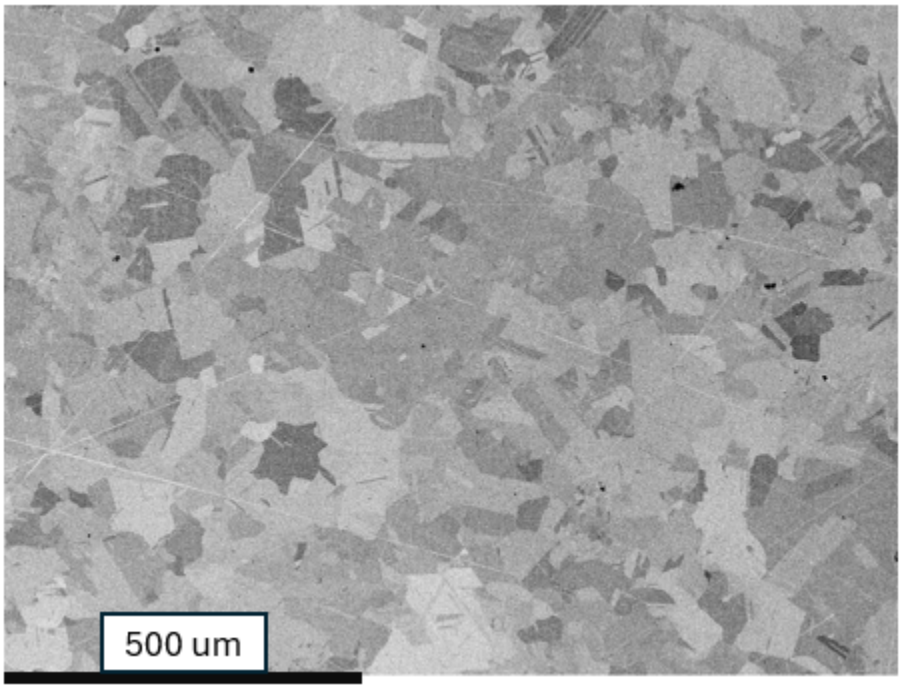

Figure 4.2 SEM/BSE image (100x) of microstructure of baseline HT vertical build IN718 specimen in XY plane.

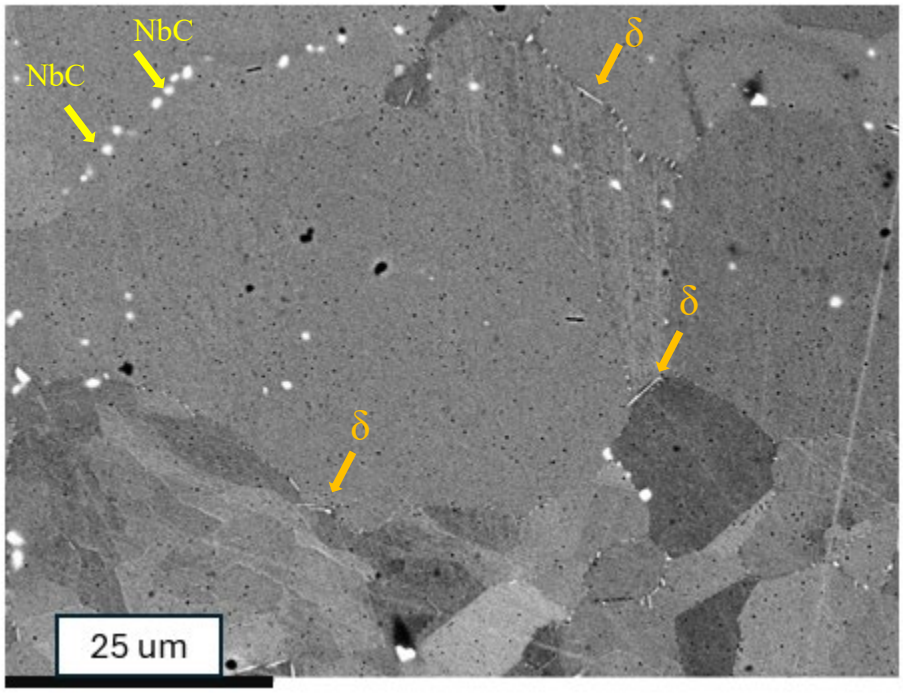

(a)

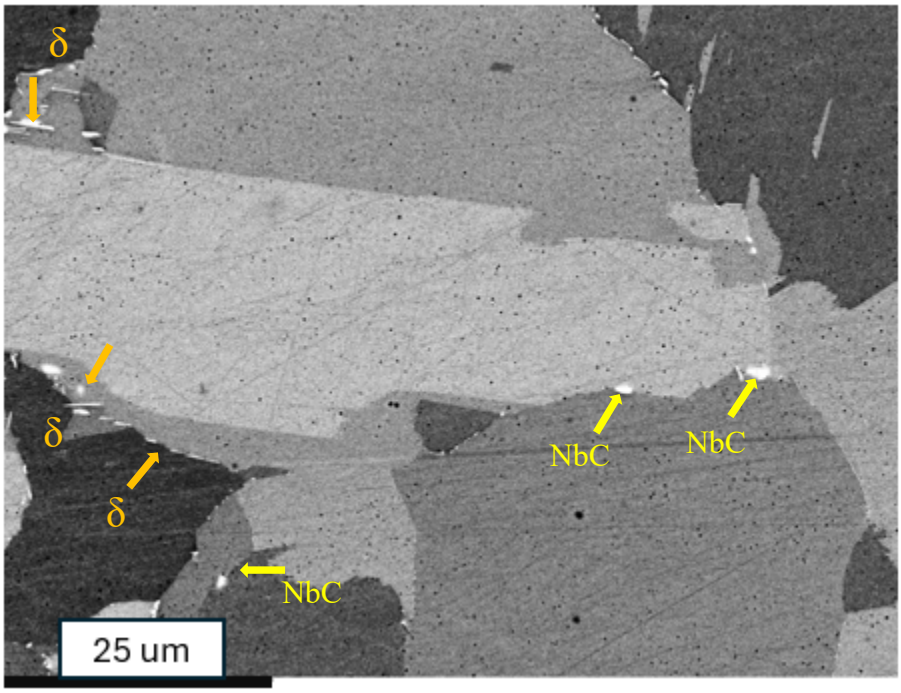

(b)

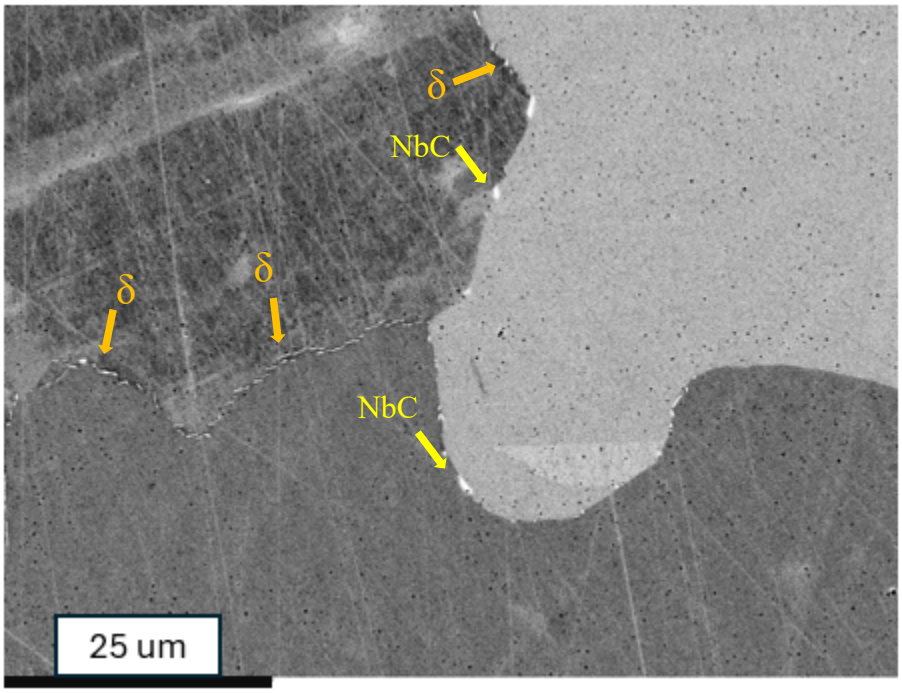

(c)

Figure 4.3 SEM/BSE images (1500x) of delta phase and carbides in XY plane for HT IN718 samples from (a) baseline vertical (b) lean C horizontal and (c) lean C vertical build.

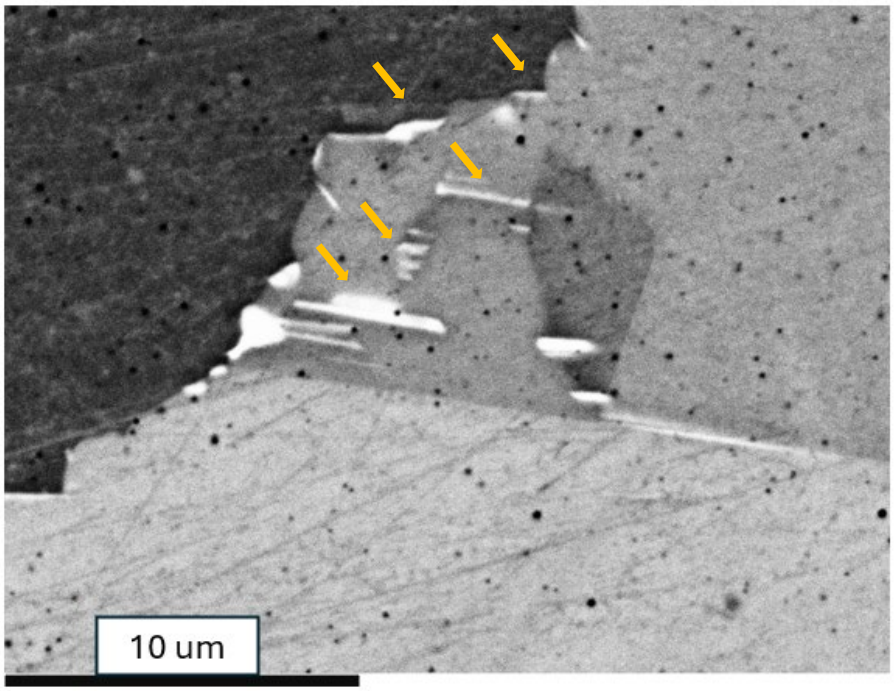

(a)

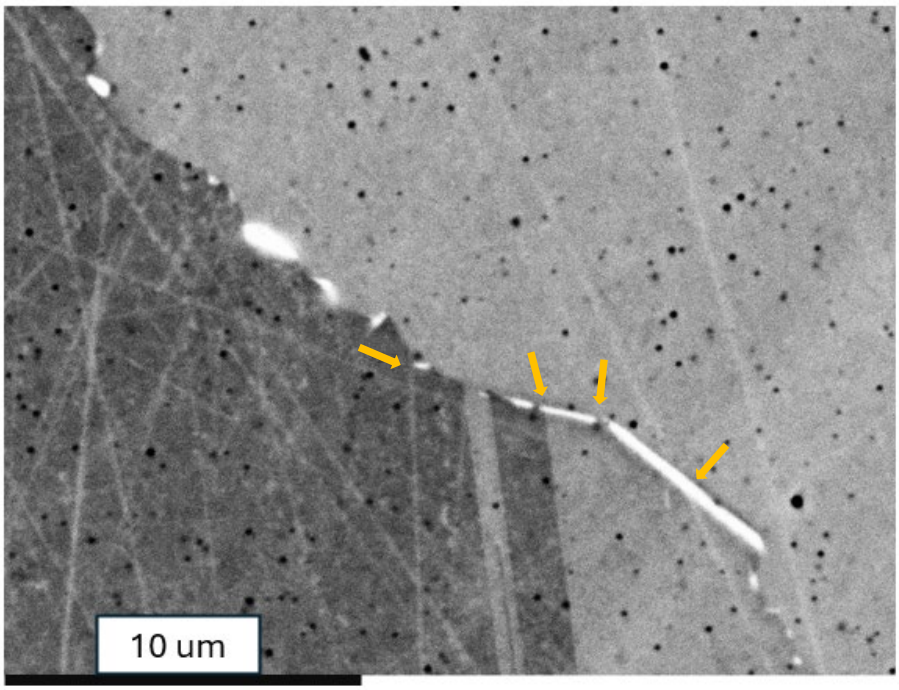

(b)

Figure 4.4 SEM/BSE images (5000x) of lean C HT specimens XY build plane with coarse acicular δ phase formation at grain boundaries from (a) horizonal and (b) vertical build.

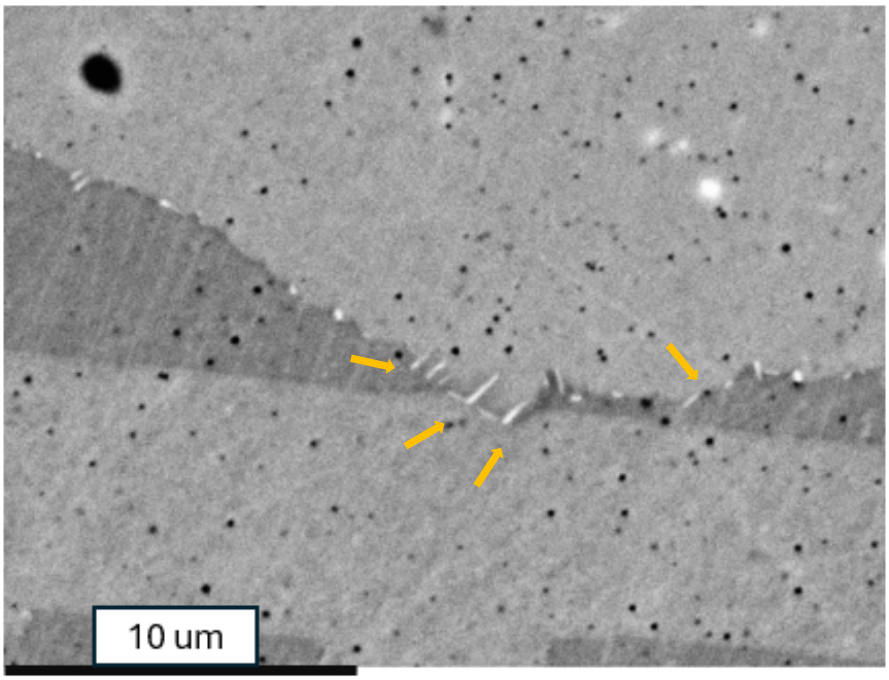

Figure 4.5 SEM/BSE image (5000x) of baseline HT specimens XY build plane with acicular δ phase formation at grain boundaries.

Table 4.3 summarizes the void size analysis from the polished optical microscopy images. The measurements taken include area fraction of the image as well as average size, and standard deviation, and feret diameter. Figure 4.6 shows the difference between as built and HT specimens for the baseline; lean C had the same results. The as built specimen void average area percentage for both the baseline vertical and lean C horizontal both averaged 3.0 ± 0.3%.

Table 4.2 Summary of void analysis after HT for IN718 specimens.

	# of Images	Count	% Area	Average Size (μm)
Baseline - Vertical - XY	6	99	0.042	27 ± 37
Baseline - Vertical - Z	6	92	0.060	22 ± 21
Lean C - Vertical - XY	6	101	.079	28 ± 19
Lean C - Vertical - Z	6	98	.044	26 ± 32
Lean C - Horizonal - XY	5	118	.097	30 ± 45
Lean C - Horizonal - Z	4	95	0.139	43 ± 35

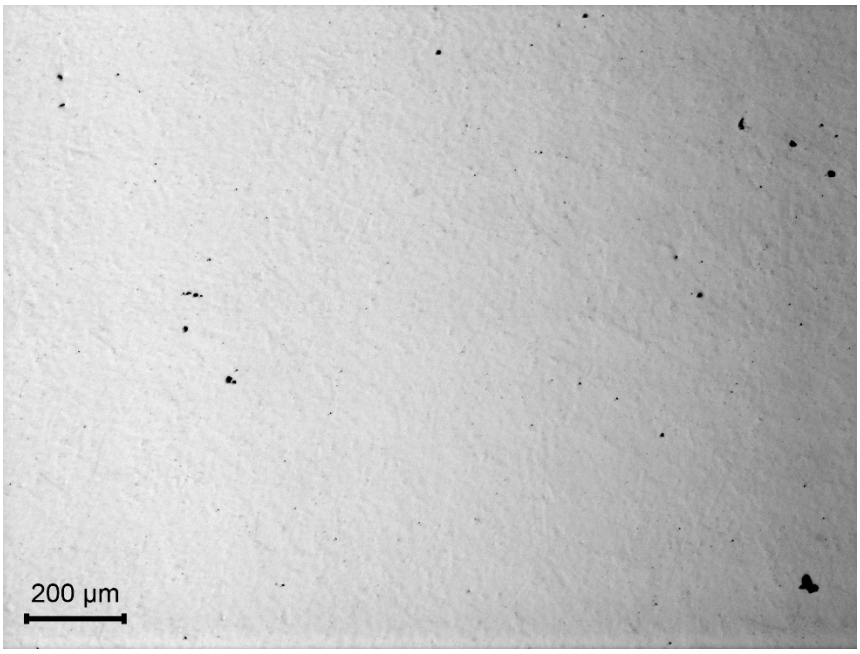

(a)

(b)

Figure 4.6 Optical microscopy images for void analysis with 5x objective of (a) baseline HT vertical and (b) lean C HT vertical build.

4.2 Tensile Testing Results

The tensile properties for all specimens tested are summarized in Table 4.4 and graphically represented with Figure 4.7.

Table 4.3 Mechanical properties for Inconel specimens.

	Number of Samples	YS (MPa)	UTS (MPa)	Elongation (%)
Baseline Vertical	4	1148 ± 2	1299 ± 6	17.7 ± 0.3
Lean C Vertical	2	1145 ± 3	1302 ± 6	16.7 ± 0.1
Lean C Horizontal	3	1163 ± 8	1314 ± 9	17.8 ± 0.2
Baseline As Built	3	773 ± 56	969 ± 12	25.6 ± 3.7
Lean C As Built	3	808 ± 4	1040 ± 2	23.3 ± 0.2
Wrought (solutionized)	4	691 ± 73	976 ± 14	26.2 ± 3.4

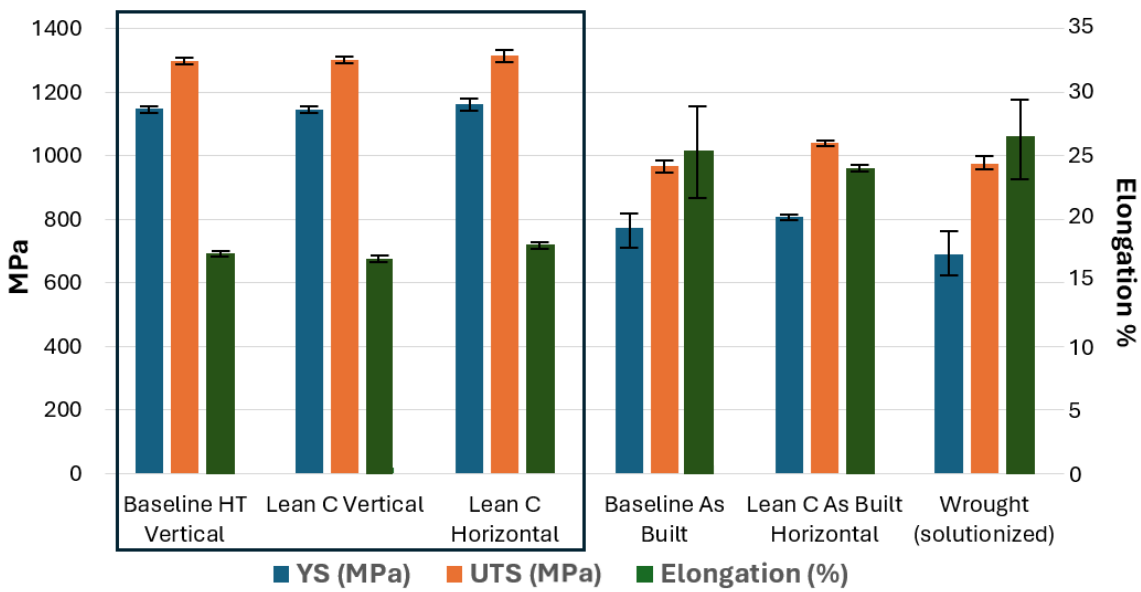

Figure 4.7 Mechanical properties for Inconel specimens.

4.3 Phase Analysis Results

The phases present were evaluated on the basis of XRD for crystal structure. The major peak shown is associated with the gamma phase (γ) and the minor peaks identified were for carbides and Laves phases. All phases are indexed with the PDF files from

International Center for Diffraction Data (ICDD) is given in Table 4.4 and Figure 4.8 compare the XRD data for the HT baseline and lean C specimens as well as the as built specimens. Figure 4.9 primarily shows the major peak for Ni, but indicates where the expected peaks for NbC, delta phase and Laves phase are along the 2-theta axis. The minor phases have very small peaks when compared to the intensity of the Ni peak. The γ matrix exhibits a major peak associated with face centered structure Ni in the 111 diffraction plane. Overlapping of minor strengthening phases, γ' and γ'', with the Ni peak occurs and will be further explored in the discussion chapter. Figure 4.10, Figure 4.11, and Figure 4.12 show the XRD for peaks for Ni, Carbides, Laves phase, and Delta phases for baseline and lean C samples, identifying the minor phases.

Table 4.4 ICDD PDF numbers for corresponding phase.

Name	PDF #
Gamma (γ)	01-004-0850 [49]
Gamma prime (γ')	04-012-8012 [50]
Gamma double prime (γ'')	04-012-8012 [50]
Delta (δ)	00-015-0101 [52]
Laves	04-004-7304 [52]
Carbides	00-038-1364 [53]
Ni	01-004-0850 [49]

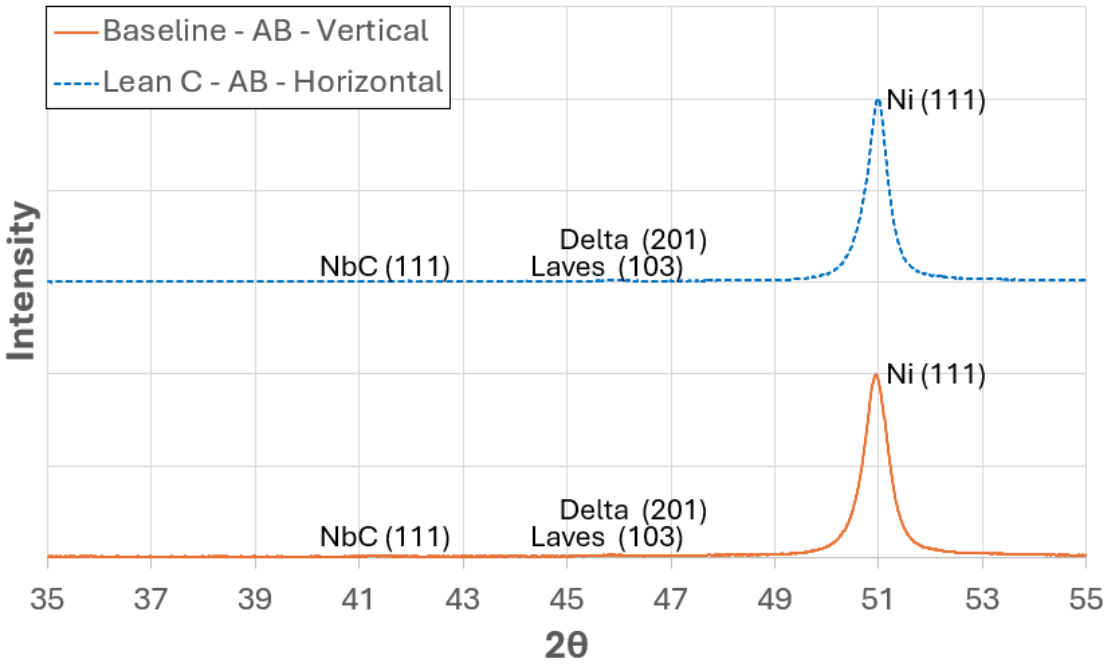

(a)

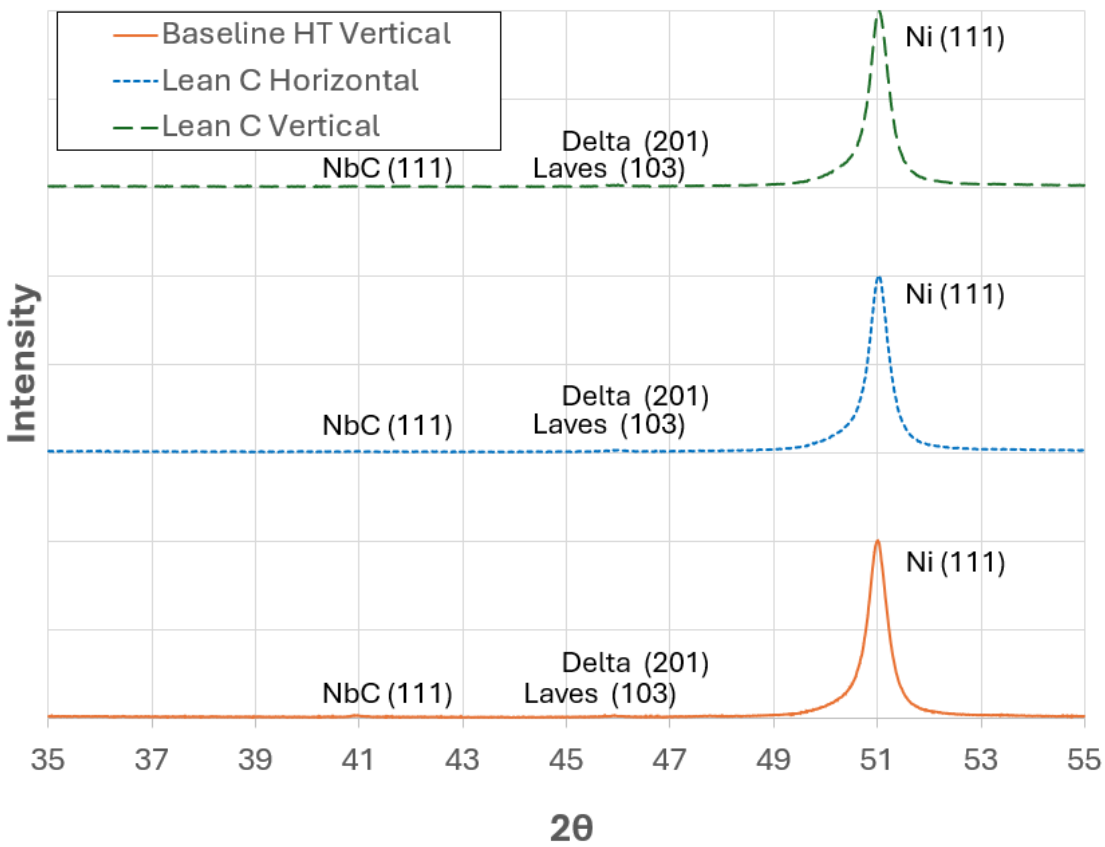

(b)

Figure 4.8 XRD analysis of IN718 for (a) as built and (b) HT.

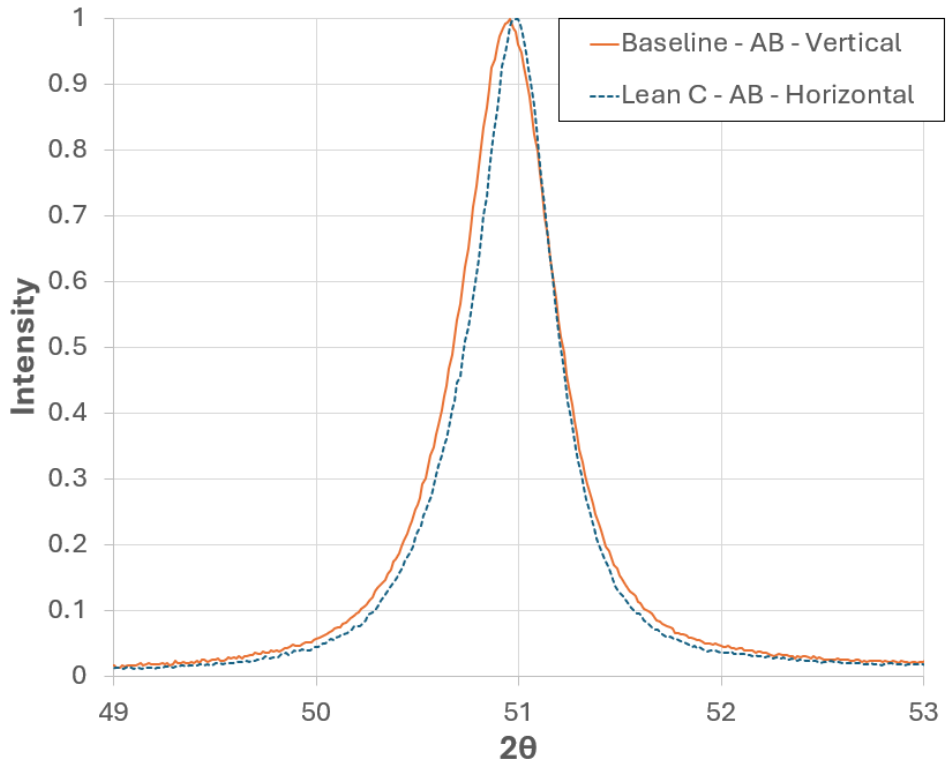

(a)

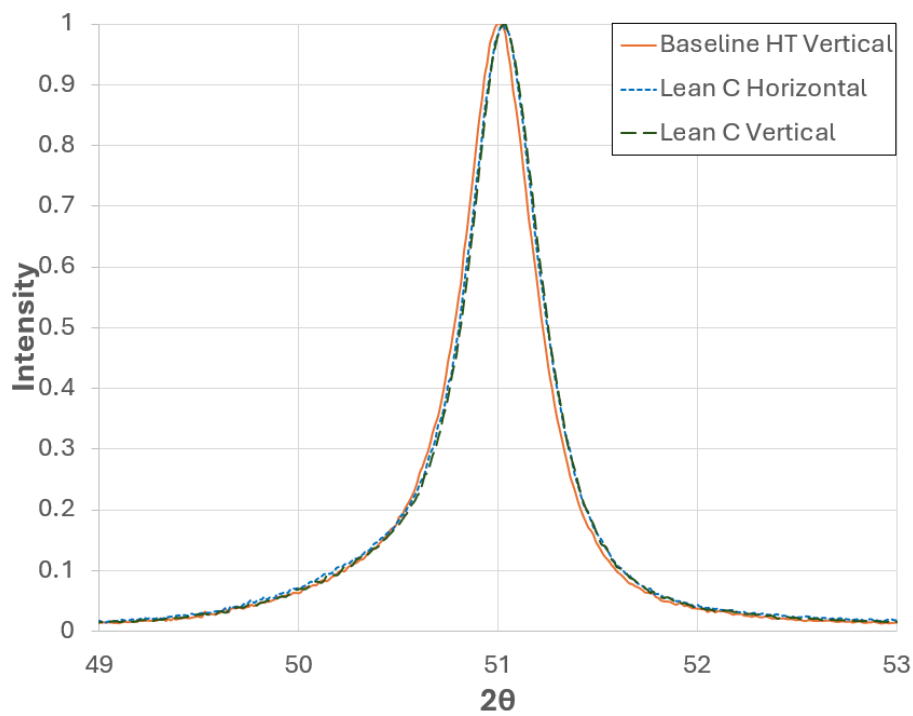

(b)

Figure 4.9 XRD analysis for Ni peak with range of 49-52° for (a) as built and (b) HT.

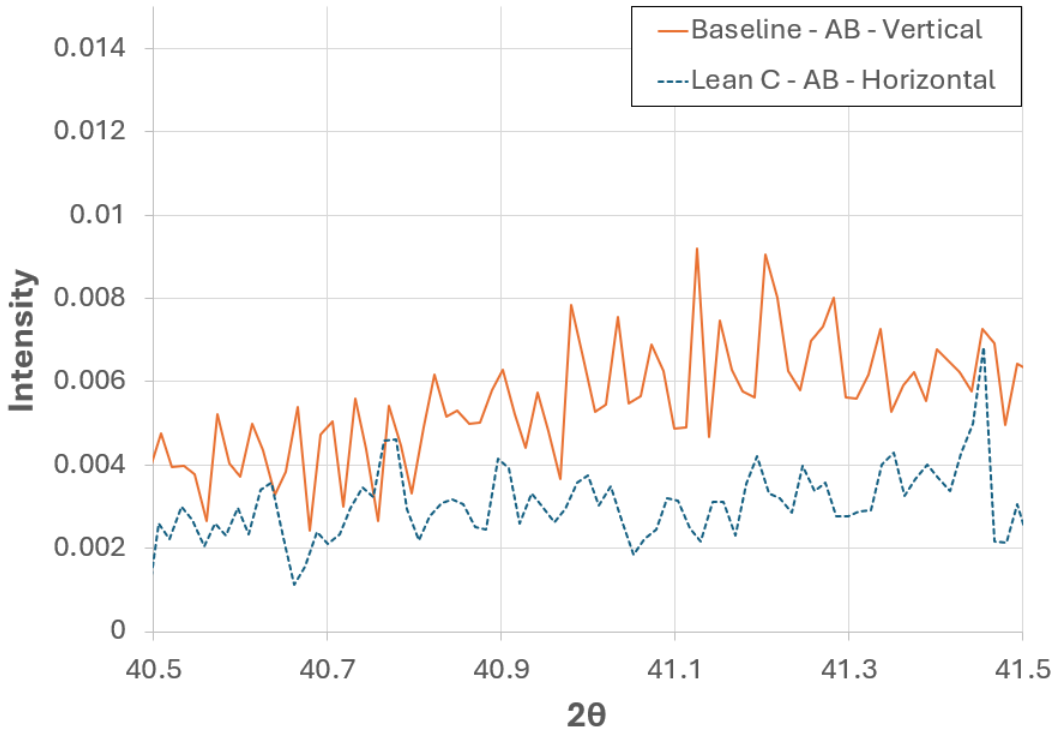

(a)

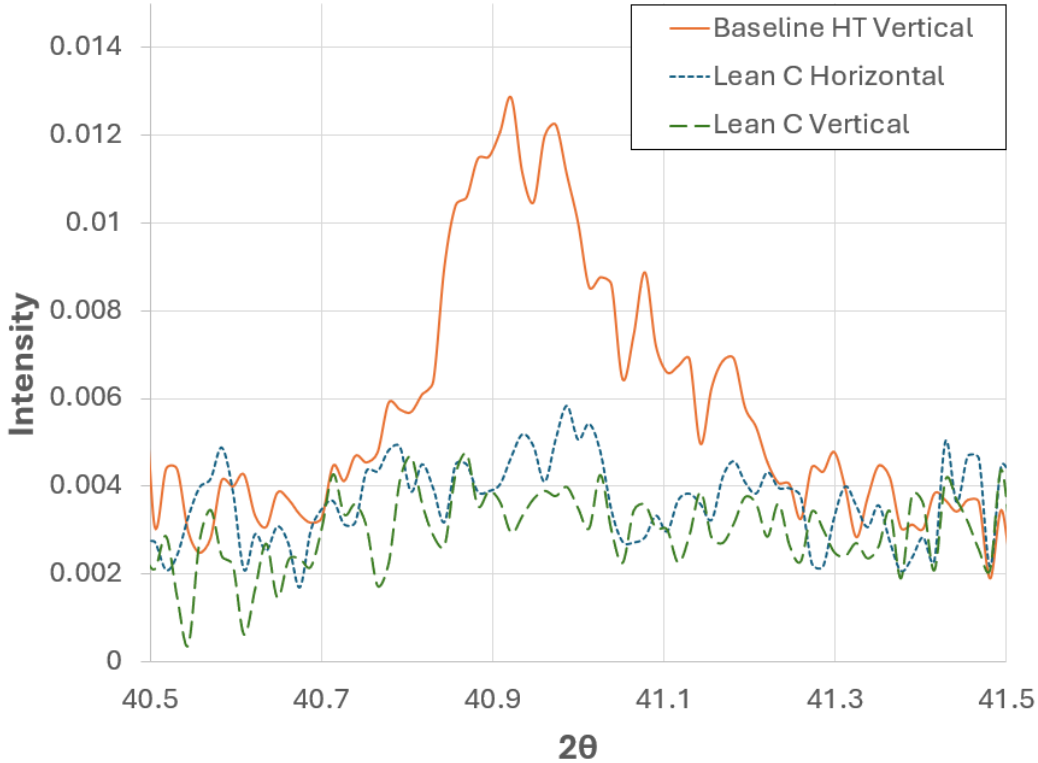

(b)

Figure 4.10 XRD analysis for NbC peak with range of 40.5-41.5° for (a) as built and (b) HT.

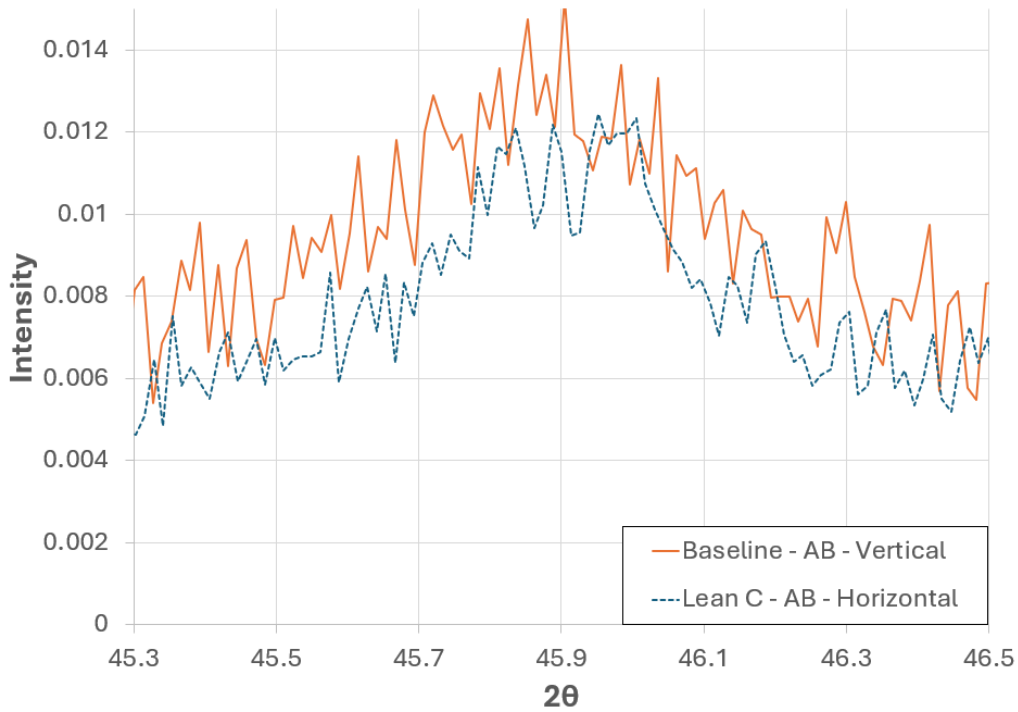

(a)

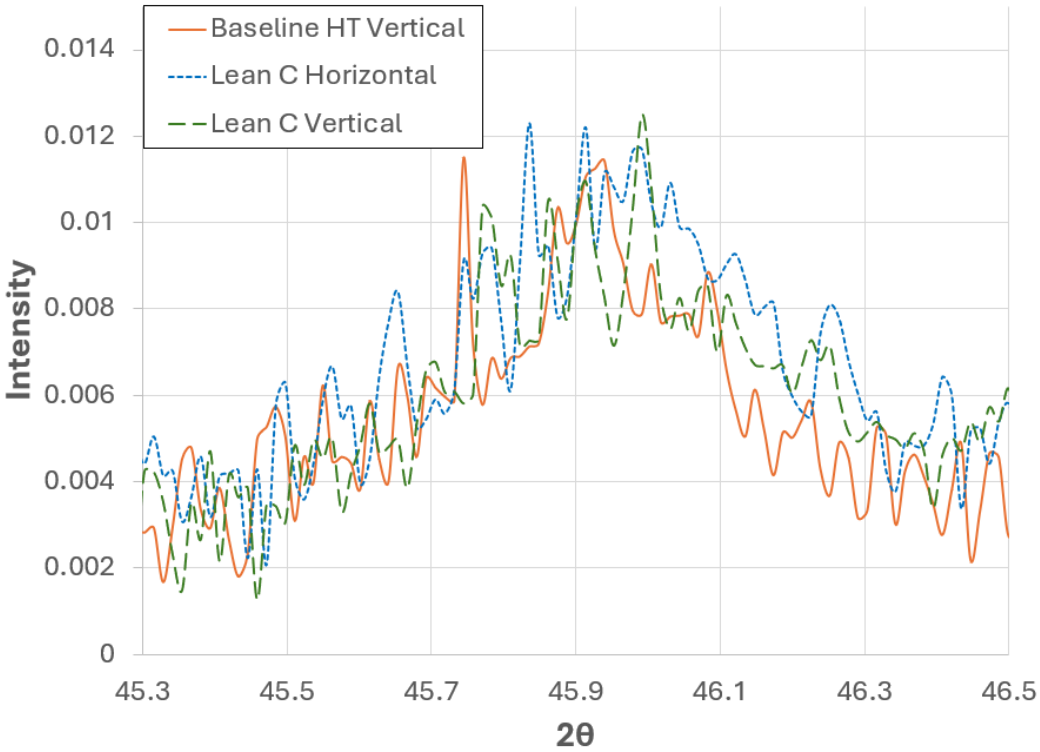

(b)

Figure 4.11 XRD analysis for Laves phase peak with range of 45.3-46.5° for IN718 (a) as built and (b) HT.

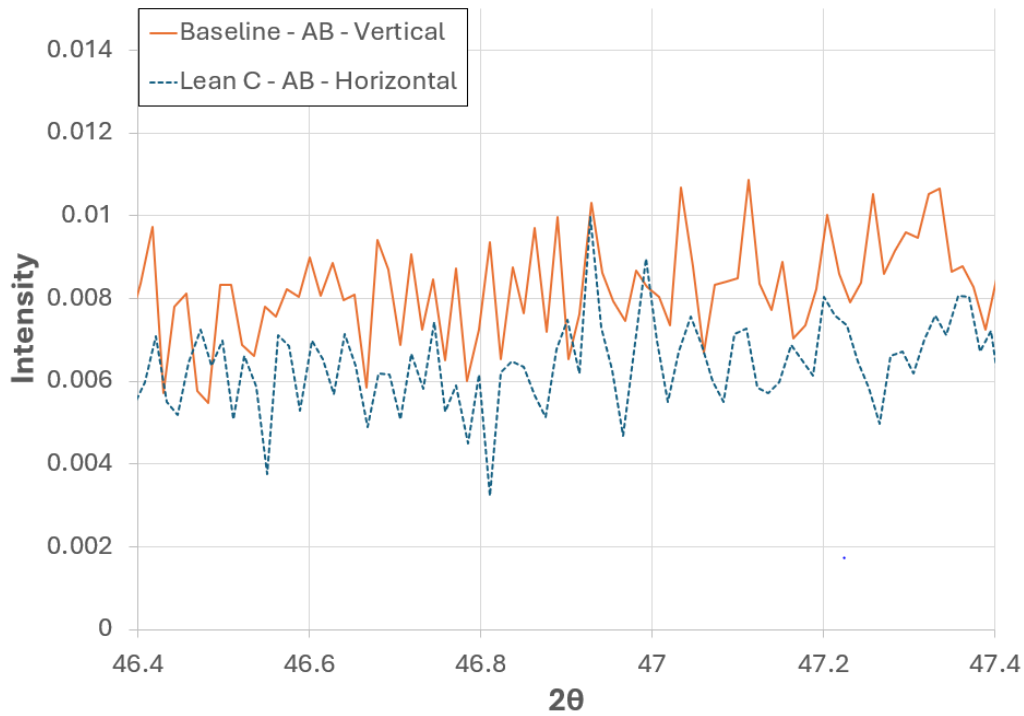

(a)

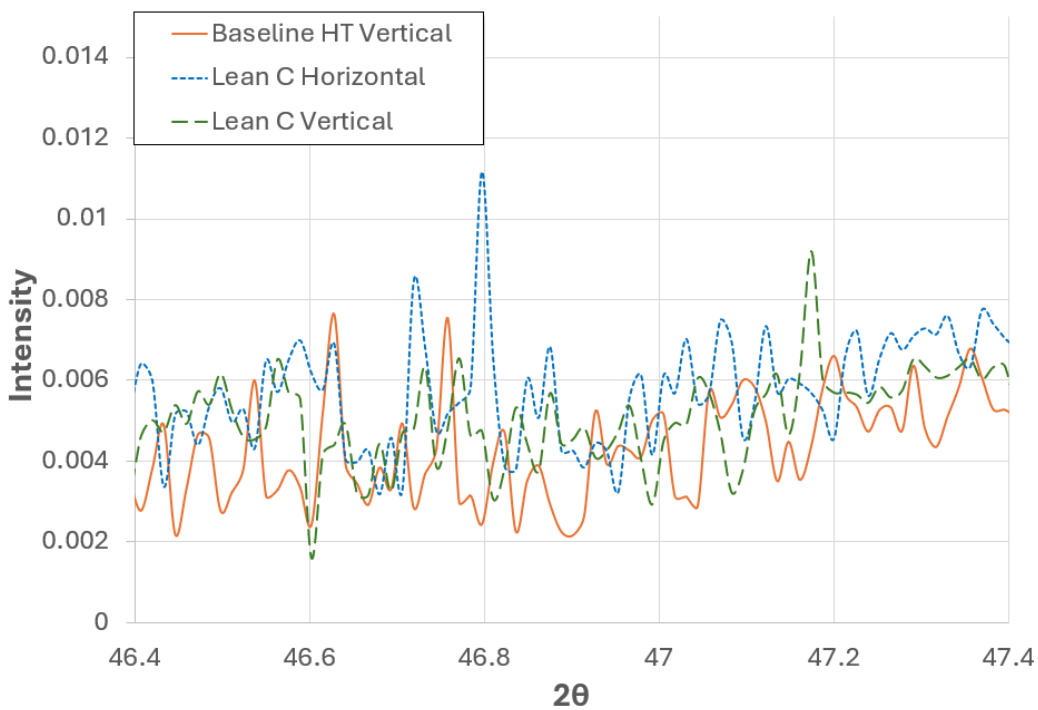

(b)

Figure 4.12 XRD Analysis for δ phase peak with range of 46.4-47.4° for IN718 (a) as built and (b) HT**.**

Chapter 5. Discussion

Using a 90% confidence interval, there was no statistical difference in the grain sizes between the HT specimens, which include the baseline vertical, lean C vertical, and lean C horizontal builds. Grain sizes can be seen in Table 4.2. Literature reports that reduction in carbon leads to a reduction in total amount of NbC carbides [54]. The reduced total number of carbides is also supposed to be correlated to an increase in the grain size [54][35][21]. In a similar study, using SEM imaging to determine area%, NbC accounted for 1.40% of the area in the baseline (.04 wt% C) and 0.35% in the lean (.01 wt% C) [35]. A reduction from 0.04 wt% to 0.01 wt% has been reported to allow for those samples to have larger grains, increasing from 50.9 µm to 77.3 µm [35].

In a different study about the effects of reducing the carbon content found similar results. That IN718 was produced using vacuum induction melting plus electro-slag remelting, then high temperature homogenizing treatment [21]. After this, their specimens were solutionized and dual aged [21]. That study looked at three different carbon contents which were, 0.027 wt% C, 0.0098 wt% C, and .0029 wt% C. Their reported grain sizes were 54.6 µm, 58.1 µm, and 75.1 respectively [21].

The Hall-Petch equation is $\sigma_y = \sigma_0 + kD^{-1/2}$. σ_y is yield strength, σ_0 is frictional stress required for dislocations, k is the H-P slope, and D is grain size [55]. Applying the H-P equation to grain size, the expected result would be to have an increase in yield strength as the grain size decreases, but that was not the case with both studies mentioned. The first study where the baseline had an average grain size 50.9 µm, and the lean C had

an average grain size of 77.3 μm, had different yield strengths. The reported yield strength for the baseline was 1041.8 ± 4.8 MPa and 1161.1 ± 11.0 MPa for the lean C [35]. The other study did not report exact numbers, but they did show a graph. Based on approximation, their yield strengths for the 0.027 wt% C samples was 1150 MPa, 0.0098 wt% C samples was 1140 MPa, and .0029 wt% C samples was 1100 MPa [21]. The second study had different yield strength results than the first. The lowest amount of C was the weakest of the three. They concluded the precipitation of NbC could improve the strength of IN718 to a certain extent [21].

Comparing the grain sizes with the H-P equation and relationships, the larger grains should be weaker, but they are not in the first study. The second study concluded that some carbides are needed for strengthening IN718 [21]. The conclusion drawn is that in IN718, although grain size is important for strength, grain size is not the primary strengthening mechanism. The strengthening precipitates γ' and γ" have a greater influence than grain size on strength.

Grain growth is also influenced by δ phase. NbC and δ phase inhibit grain growth and prevent grain boundary sliding [56]. Nb is used in all phases present in IN718, excluding the γ matrix. Laves phase requires 10-12% of the Nb, δ phase requires 6-8% of the Nb, γ" needs 4% of the Nb, and γ' can form at Nb levels below 4% of the Nb [56].

The δ phase forms during solidification or precipitation. In precipitation, acicular δ occurs due to achieving appropriate solutionizing temperature and time to drive the existing delta into solution and allowing it to precipitate along the grain boundaries, which appears to be the case for the baseline. The lean C conditions may have not been favorable to drive the existing δ phase back into the solution, thus the existing δ phase coarsened. The

solutionizing time and temperature was the same for all specimens in this study [29][39][57]. Referring to the TTT diagram, δ phase occurs at temperatures greater than 650°C. δ phase over 4% at grain boundaries can efficiently inhibit grain growth during heat treatments and working [39]. In a different study, spray formed and wrought IN718 were solution treated and characterized before and after aging. After solution treatment, δ phase dissolved completely in the spray form and δ phase, and less than 1 vol% in the wrought remained [57]. After the solution treatment, the grains grew by 10% [57]. Once aging occurred, grains returned to their original size. The study concluded δ phase can contribute to grain growth inhibition, but in its absence other precipitates such as NbC also inhibit grain growth [57].

The lack of difference in grain sizes in this current study would suggest that there may have been a tradeoff between grain boundary growth inhibiting phases, specifically NbC and δ phase. With XRD, NbC was only observed in the baseline HT specimen, meeting the detection limit. Concluding, the volume fraction was higher in than the lean C HT specimens, which was not detectable. The grain size was expected to be larger in the lean carbon samples due to theorizing that less NbC would be present to pin grain boundaries thereby resulting in larger grains, but this was not found [38]. The δ was qualitatively coarser in the lean C specimens, which may have resulted in grain growth inhibition.

The process history also influences the grain size in AM IN718 [39]. But the heat treated specimens in this study had the same manufacturing and processing, the only structural difference was the compositional carbon on the powder, which also carried over to the final composition of the bulk as seen in Table 3.1. The .01 wt% carbon is the lower

limit possible to produce due to trace amounts of carbon found in the raw materials used for powder production in commercial atomization practices [35].

The void analysis for all specimens confirmed that the HIP process was effective in reducing voids and increasing density. The void average went from ≈ 3% to under ≈ 0.1% for all specimens, as seen in Table 4.3 and Figure 4.6. HIP processes are designed to improve the density of the specimens. In AM IN718, temperature should be higher than 1150°C to obtain significant reduction in voids [58]. The voids may be caused by trapped gasses or embedded in the powder particles [58].

Phase analysis with XRD showed only the baseline HT specimen had a peak for NbC as observed in Figure 4.10. The baseline specimen had a peak intensity of about 1.3%. The lack of a peak for NbC in the lean C and as built specimens does not mean NbC is not present, but rather the volume fraction or the size of the phase may be below the detection limit for XRD. XRD is a bulk technique which is dependent on the volume fraction and phases present. Detection limits for nanoparticles is in a reported range of 2–2.5 nm [59]. Volume fractions with particle concentrations less than 1-4 wt% will not be detected [60]. NbC was observed in all specimens in the SEM based on morphology and location. Measured with SEM images, the average sizes of NbC particle in all specimens range from 1-2 μm. NbC meets the nanoparticle size detection limit of 2 - 2.5 nm in all specimens. Therefore, both lean C HT specimens and as built specimens did not meet the volume fraction threshold.

All samples had the Ni peak, which was normalized and associated with the γ matrix. The Ni peak reflects the FCC structure of the γ matrix. No peaks associated with γ' or γ'' were seen in any of the samples due to their expected overlap with the matrix since

the crystal structures are similar.

The Laves phase was observed for all specimens with XRD, as identified in Figure 4.11. Laves had intensities of about 1.2% in the HT specimens and 1.4% in the as built specimens. Referring to the TTT diagram with heat treatment schedule, Figure 3.5, Laves phase was not reached during the solution phase of the heat treatment. Laves phase did not fully dissolve either. Thus, Laves phase was not precipitated, it formed during solidification.

The δ phase was not observed with XRD for any specimens. This may be due to the small size or amount present which is below the limit of XRD detection. δ phase was observed in the SEM and confirmed based on morphology and location along the grains.

Chapter 6. Summary

This study evaluated the effects of reducing carbon content in the processing of superalloy Inconel 718. Specimens were fabricated into cylinders with a diameter of 12.7 mm and a length of 90 mm using L-PBF. Heat treated specimens were produced in accordance with Table 3.2. The baseline as built specimens were built in the vertical direction and the as built lean C specimens were built in the horizontal direction. The HIP temperature is above the Laves and δ phase solvus temperatures. The specimens were characterized through elemental analysis, microstructural analysis, phase analysis with XRD, and mechanical properties.

- The difference in C content between the baseline powder and bulk was .04 wt% C for the baseline and .01 wt% C for the lean specimens. The vendor determined this with ICP.
- With a 90% confidence interval, no statistical difference was found in grain size of the HT baseline and HT lean C specimens. This is likely due to a tradeoff between phases pinning grain boundaries. In the baseline HT, NbC was observed present with XRD, meaning the volume percent was high enough to be detected. NbC would be the primary grain pinning phase in the baseline and δ in the lean C specimens.
- HIP was effective in reducing voids and increasing density of the specimens. After HIP, void size between HT specimens had no statistical differences with a 90% confidence interval.

- No statistical difference observed with tensile properties of baseline and lean C specimens with a 95% confidence interval. Given the lack of difference in grain size, the result is logical.
- The NbC phase was only measurable in XRD for the baseline HT specimens. NbC was observed with SEM imaging for all specimens, which was determined by morphology.
- The Laves phase was identified in all specimens using XRD analysis. The HT schedule did not reach the Laves phase curve on the TTT diagram, therefore some amount of Laves phase formed during solidification.

Chapter 7. Future Work

Literature evidence suggests that varying the carbon content should result in different grain sizes for the lean C and baseline specimens, but this behavior was not observed. To test the influence of δ phase and NbC on grain boundary formation, changing the solutionizing time from 1 hour to 30 minutes would limit the amount of time δ phase can precipitate. Keeping all else the same with the heat treatment parameters, this could give a different resulting grain size. Since the δ phase was qualitatively coarser in the lean C, reducing the amount by varying the solutionizing time of the heat treatment will lead to understanding whether there was a tradeoff between NbC and δ phase at controlling grain growth.

For further study, the wrought should be fully characterized and compared to the as built specimens since it was solutionized. The wrought could theoretically have smaller grains since it has been worked. The smaller grains would show a decrease in strength with an increase in ductility. The wrought should also be heat treated to see how it compares to the AM HT specimens.

To fully appreciate the differences between lean C and the baseline, baseline HT horizontal build, baseline as built horizontal build, and lean C as built vertical build should be fabricated with at least 4 specimens of each to conduct tensile testing as well as 3 specimens of each to conduct full characterization. Experiments should be executed as stated in this study. Results can be used to fully characterize the difference in heat treated lean C and baseline, as well as the as built lean C and baseline, and wrought. More fully

characterized differences between lean C and baseline would also be more fully characterized with SEM imaging. The images should be used to analyze area fractions of NbC and δ phase. This information would allow us to fully appreciate the difference in those phases between the baseline and lean C specimens.

References

[1] Keiser, D.D., and H.L. Brown. (1976). Review of the Physical Metallurgy of Alloy 718. Feb. 1976, https://doi.org/10.2172/4016087.

[2] Hosseini, E., & Popovich, V. A. (2019). A review of mechanical properties of additively manufactured Inconel 718. In Additive Manufacturing (Vol. 30, p. 100877). Elsevier BV. https://doi.org/10.1016/j.addma.2019.100877

[3] Wagner, H. J., & Hall, A. M. (1965). Physical metallurgy of alloy 718 (Vol. 217). Defense Metals Information Center, Battelle Memorial Institute.

[4] ASTM 52900-21, Additive Manufacturing – General principles – Fundamentals and vocabulary, ASTM International, West Conshohocken, PA, 2021.

[5] Wohlers, T., Gornet, T. (2015). History of additive manufacturing. In Wohlers Report 2015 (pp. 1-35).

[6] Wohlers, T., Gornet, T., Mostow, N., Campbell, I., Diegel, O., Kowen, J., Huff, R., Stucker, B., Fidan, I., Doukas, A., Drab, B., Drstvenšek, I., Eitsert, N. (2023). History of Additive Manufacturing. In SSRN Electronic Journal. Elsevier BV. https://doi.org/10.2139/ssrn.4474824

[7] Viereckl, R. J., Gould, M., Petry, V., Dodd, R., Marguerettaz, X., Des Roches, S. (2018). Formulating for 3D printing (SLA). RadTech UV+ EB.

[8] Hull, C. W. (1986). United States of America Patent No. US4575330 A. U.S. Patent and Trademark Office.

[9] Sachs, E. M., Cima, M. J., Williams, P. A. (1993). US Patent No. 5204055A. U.S. Patent and Trademark Office

[10] Razavykia, A., Brusa, E., Delprete, C., Yavari, R. (2020). An Overview of Additive Manufacturing Technologies—A Review to Technical Synthesis in Numerical Study of Selective Laser Melting. In Materials (Vol. 13, Issue 17, p. 3895). MDPI AG. https://doi.org/10.3390/ma13173895

[11] Gradl, P. R. (2020, December). AM Processes Part 2: Principles of Directed Energy Deposition. In ASTM Training: AM processes: Part 2–Principles of Directed Energy Deposition.

[12] Conner, B. P., Manogharan, G. P., Martof, A. N., Rodomsky, L. M., Rodomsky, C. M., Jordan, D. C., Limperos, J. W. (2014). Making sense of 3-D printing: Creating a map of additive manufacturing products and services. In Additive Manufacturing (Vols. 1–4, pp. 64–76). Elsevier BV. https://doi.org/10.1016/j.addma.2014.08.005

[13] Berman, B. (2012). 3-D printing: The new industrial revolution. In Business

Horizons (Vol. 55, Issue 2, pp. 155–162). Elsevier BV. https://doi.org/10.1016/j.bushor.2011.11.003

[14] Frazier, W. E. (2014). Metal Additive Manufacturing: A Review. In Journal of Materials Engineering and Performance (Vol. 23, Issue 6, pp. 1917–1928). Springer Science and Business Media LLC. https://doi.org/10.1007/s11665-014-0958-z

[15] Oliveira, J. P., LaLonde, A. D., Ma, J. (2020). Processing parameters in laser powder bed fusion metal additive manufacturing. In Materials & Design (Vol. 193, p. 108762). Elsevier BV. https://doi.org/10.1016/j.matdes.2020.108762

[16] Yap, C. Y., Chua, C. K., Dong, Z. L., Liu, Z. H., Zhang, D. Q., Loh, L. E., & Sing, S. L. (2015). Review of selective laser melting: Materials and applications. In Applied Physics Reviews (Vol. 2, Issue 4). AIP Publishing. https://doi.org/10.1063/1.4935926

[17] Vandzura, R., Simkulet, V., Gelatko, M., Hatala, M., & Mitalova, Z. (2023). Effect of Hardening Temperature on Maraging Steel Samples Prepared by Direct Metal Laser Sintering Process. In Machines (Vol. 11, Issue 3, p. 351). MDPI AG. https://doi.org/10.3390/machines11030351

[18] Paulonis, D. F., and Schirra, J. J. (2001)., Alloy 718 at Pratt & Whitney: Historical perspective and future challenges. Superalloys 718, 625, 706 and Various Derivatives, Jan. 2001.

[19] Nabavi, B., Goodarzi, M., Khan, A.K. (2019). Metallurgical Effects of Nitrogen on the Microstructure and Hot Corrosion Behavior of Alloy 718 weldment, Materials Characterization, Volume 157, 2019, 109916, ISSN 1044-5803, https://doi.org/10.1016/j.matchar.2019.109916.

[20] Sundararaman, M., Mukhopadhyay, P., Banerjee, S. (1997). Carbide Precipitation in Nickel Base Superalloys 718 and 625 and Their Effect on Mechanical Properties. In Superalloys 718, 625, 706 and Various Derivatives (1997). Superalloys. TMS. https://doi.org/10.7449/1997/superalloys_1997_367_378

[21] Zheng, W., Wei, X., Song, Z., Yong, Q., Feng, H., Xie, Q. (2015). Effects of Carbon Content on Mechanical Properties of Inconel 718 alloy. In Journal of Iron and Steel Research International (Vol. 22, Issue 1, pp. 78–83). Springer Science and Business Media LLC.

[22] Zhang, Y. N., Cao, X., Wanjara, P., Medraj, M. (2013). Oxide Films in Laser Additive Manufactured Inconel 718. In Acta Materialia (Vol. 61, Issue 17, pp. 6562–6576). Elsevier BV. https://doi.org/10.1016/j.actamat.2013.07.039

[23] ASTM International. (2021). ASTM F3055-14a (2021): Standard Specification for Additive Manufacturing Nickel Alloy (UNS N07718) with Powder Bed Fusion. ASTM Standard. Retrieved from https://www.document-

center.com/standards/show/ASTM-F3055

[24] Bean, G. E., McLouth, T. D., Witkin, D. B., Sitzman, S. D., Adams, P. M., & Zaldivar, R. J. (2019). Build Orientation Effects on Texture and Mechanical Properties of Selective Laser Melting Inconel 718. In Journal of Materials Engineering and Performance (Vol. 28, Issue 4, pp. 1942–1949). Springer Science and Business Media LLC. https://doi.org/10.1007/s11665-019-03980-w

[25] Anzini, E., Glaenzer, N., Mignanelli, P. M., Hardy, M. C., Stone, H. J., Pedrazzini, S. (2020). The Effect of Manganese and Silicon Additions on the Corrosion Resistance of a Polycrystalline Nickel-Based Superalloy. In Corrosion Science (Vol. 176, p. 109042). Elsevier BV. https://doi.org/10.1016/j.corsci.2020.109042

[26] Sims, C. T., Hagel, W. C. (1994). The Superalloys. In Superalloys 1994 (pp. 89-98). The Minerals, Metals & Materials Society. Retrieved from https://www.tms.org/Superalloys/10.7449/1994/Superalloys_1994_89_98.pdf

[27] Mitchell, A., Schmalz, A. J., Schvezov, C., Cockroft, S. L. (1994). The Precipitation of Primary Carbides in Alloy 718. In Superalloys 718, 625, 706 and Various Derivatives (1994). Superalloys. TMS. https://doi.org/10.7449/1994/superalloys_1994_65_78

[28] Yen, Y., Su, J., & Huang, D. (2008). Phase equilibria of the Fe–Cr–Ni ternary systems and interfacial reactions in Fe–Cr alloys with Ni substrate. In Journal of Alloys and Compounds (Vol. 457, Issues 1–2, pp. 270–278). Elsevier BV. https://doi.org/10.1016/j.jallcom.2007.03.053

[29] Ferreri, N. C., Vogel, S. C., Knezevic, M. (2020). Determining Volume Fractions of γ, γ′, γ″, δ, and MC-Carbide Phases in Inconel 718 as a Function of its Processing History Using an Advanced Neutron Diffraction Procedure. In Materials Science and Engineering: A (Vol. 781, p. 139228). Elsevier BV. https://doi.org/10.1016/j.msea.2020.139228

[30] Slama, C., Abdellaoui, M. (2000). Structural characterization of the aged Inconel 718. In Journal of Alloys and Compounds (Vol. 306, Issues 1–2, pp. 277–284). Elsevier BV. https://doi.org/10.1016/s0925-8388(00)00789-1

[31] Emanuelli, L., Deirmina, F., Pellizzari, M. (2023). Heat treatment behavior of IN718 superalloy fabricated by laser-powder bed fusion. In Materials Characterization (Vol. 199, p. 112788). Elsevier BV. https://doi.org/10.1016/j.matchar.2023.112788

[32] Thompson, R.G.; Dobbs, J.; Mayo, D. (1986) The Effect of Heat Treatment on Microfissuring in Alloy 718. Weld J. 1986, 65, 299–304.

[33] ASTM International. (2009). AMS5663M: Nickel Alloy, Corrosion and Heat-Resistant, Bars, Forgings, and Rings 52.5Ni - 19Cr - 3.0Mo - 5.1Cb (Nb) - 0.90Ti

- 0.50Al - 18Fe Consumable Electrode or Vacuum Induction Melted 1775 °F (968 °C) Solution and Precipitation Heat Treated. SAE Standard. Retrieved from https://doi.org/10.4271/AMS5663M

[34] A.M.S. 5662 - Nickel Alloy, Corrosion and Heat-resistant, Bars, Forgings, and Rings 52.5Ni - 19Cr - 3.0Mo - 5.1Cb (Nb) - 0.90Ti - 0.50AI - 18Fe Consumable Electrode or Vacuum Induction Melted 1775 °F (968 °C) Solution Heat Treated, Precipitation-Hardenable - UNS N07718, 2016.

[35] McLouth, T. D., Witkin, D. B., Lohser, J. R., Bean, G. E., Adams, P. M., Lingley, Z. R., & Zaldivar, R. J. (2022). Influence of reduced carbon content on microstructure and mechanical behavior of Inconel 718 prepared by laser powder bed fusion. In Additive Manufacturing Letters (Vol. 3, p. 100037). Elsevier BV. https://doi.org/10.1016/j.addlet.2022.100037

[36] Huan, Q. (2012). Review of INCONEL 718 Alloy: Its History, Properties, Processing and Developing Substitutes. Journal of Materials Engineering, 92-100.

[37] Jackman, L., Boldy, M., & Coffey, A. (1991). The influence of reduced carbon on alloy 718. Superalloys, 718(625), 261-270.

[38] Sundararaman, M., Mukhopadhyay, P. (1993). Carbide Precipitation in Inconel 718. In High Temperature Materials and Processes (Vol. 11, Issues 1–4, pp. 351–368). Walter de Gruyter GmbH. https://doi.org/10.1515/htmp.1993.11.1-4.351

[39] Deng, D. (2018). Additively Manufactured Inconel 718: Microstructures and Mechanical Properties (Vol. 1798). Linköping University Electronic Press.

[40] Bean, G. E., Witkin, D. B., McLouth, T. D., Zaldivar, R. J. (2020). Process gas influence on microstructure and mechanical behavior of Inconel 718 fabricated via selective laser melting. In Progress in Additive Manufacturing (Vol. 5, Issue 4, pp. 405–417). Springer Science and Business Media LLC. https://doi.org/10.1007/s40964-020-00133-7

[41] ASTM D8110-17 , Standard Test Method for Elemental Analysis of Distillate Products by Inductively Coupled Plasma Mass Spectrometry (ICP-MS), ASTM International, West Conshohocken, PA, 2017

[42] ASTM E1019-18 , Standard Test Methods for Determination of Carbon, Sulfur, Nitrogen, and Oxygen in Steel, Iron, Nickel, and Cobalt Alloys by Various Combustion and Inert Gas Fusion Techniques, ASTM International, West Conshohocken, PA, 2018

[43] Heo, S., Lim, Y., Kwak, N., Jeon, C., Choi, M., & Jo, I. (2024). Impact of Heat Treatment and Building Direction on Tensile Properties and Fracture Mechanism of Inconel 718 Produced by SLM Process. In Metals (Vol. 14, Issue 4, p. 440). MDPI AG. https://doi.org/10.3390/met14040440

[44] Mugwagwa, L., Yadroitsev, I., Matope, M. (2019). Effect of Process Parameters on Residual Stresses, Distortions, and Porosity in Selective Laser Melting of Maraging Steel 300. In Metals (Vol. 9, Issue 10, p. 1042). MDPI AG. https://doi.org/10.3390/met9101042

[45] Phenomount black phenolic 25 lbs. OnPoint Abrasives. (n.d.). https://onpointabrasives.com/products/phenomount-black-phenolic-25-lbs-item-no-pmb-2025

[46] Vander Voort, G., Manilova, E., & Lucas, G. M. (2004). Metallographic techniques for superalloys. Microscopy and Microanalysis, 10(S02), 690-691.

[47] Schindelin, J., Arganda-Carreras, I., Frise, E., Kaynig, V., Longair, M., Pietzsch, T., Cardona, (2012). A. Fiji: an open-source platform for biological-image analysis. Nature Methods, 9(7), 676 - 682, 2012.

[48] ASTM E8/E8M-21, Standard Test Methods for Tension Testing of Metallic Materials, ASTM International, West Conshohocken, PA, 2021

[49] International Center for Diffraction Data PDF #01-004-0850. 2019.

[50] International Center for Diffraction Data PDF #04-012-8012, 2019.

[51] International Center for Diffraction Data PDF #00-015-0101, 2011.

[52] International Center for Diffraction Data PDF #04-004-7304, 2015.

[53] International Center for Diffraction Data PDF #00-038-1364, 2007.

[54] Smith, T. M., Gabb, T. P., Kantzos, C. A., Thompson, A. C., Sudbrack, C. K., West, B., & Bowman, C. L. (2021). The effect of composition on microstructure and properties for additively manufactured superalloy 718. Journal of Alloys and Compounds, 873, 159789.

[55] Meyers, M.A. and Chawla, K.K. (2009) Mechanical Behavior of Materials. 2nd Edition, Cambridge University Press, Cambridge.

[56] Saleem, B., Dong, H. B., & Patel, V. (2020). Alloy 718 Subsea Bolt in Relation to Surface Cracking: A Microstructural Perspective. In Materials Sciences and Applications (Vol. 11, Issue 12, pp. 787–816). Scientific Research Publishing, Inc. https://doi.org/10.4236/msa.2020.1112053

[57] Azadian, S., Wei, L.-Y., Warren, R. (2004). Delta phase precipitation in Inconel 718. In Materials Characterization (Vol. 53, Issue 1, pp. 7–16). Elsevier BV. https://doi.org/10.1016/j.matchar.2004.07.004

[58] Tillmann, W., Schaak, C., Nellesen, J., Schaper, M., Aydinöz, M. E., & Hoyer, K.-P. (2017). Hot isostatic pressing of IN718 components manufactured by

selective laser melting. In Additive Manufacturing (Vol. 13, pp. 93–102). Elsevier BV. https://doi.org/10.1016/j.addma.2016.11.006

[59] Weibel, A., Bouchet, R., Boulc', F., & Knauth, P. (2005). The Big Problem of Small Particles: A Comparison of Methods for Determination of Particle Size in Nanocrystalline Anatase Powders. In Chemistry of Materials (Vol. 17, Issue 9, pp. 2378–2385). American Chemical Society (ACS). https://doi.org/10.1021/cm0403762

[60] Vyverberg, K. L., Jaeger, J. M., & Dutton, A. (2018). Quantifying Detection Limits and Uncertainty in X-ray Diffraction Mineralogical Assessments of Biogenic Carbonates. In Journal of Sedimentary Research (Vol. 88, Issue 11, pp. 1261–1275). Society for Sedimentary Geology. https://doi.org/10.2110/jsr.2018.63